ABSTRACT

Spatial Correlation of Selected Earthquakes with the Dog Valley Fault
in Northern California using LiDAR and GPS Data

Matthew P. Strasser, M.S.

Committee Chairperson: Vincent S. Cronin, Ph.D.

The 1966 M6.0 Truckee earthquake has a reported location of 39.438°N 120.160°W at ~10 km depth (Ryall et al., 1968), ~5 km southwest of the Stampede Dam, an earth-fill structure built in 1970 to impound 226,500 acre-feet of water (DWR, 2017). USBR estimates 148,400 people living downstream along the Truckee River would be affected should the Stampede Dam fail. The Truckee earthquake was attributed to the previously unrecognized Dog Valley Fault (DVF) whose surface trace has remained elusive. The Seismo-Lineament Analysis Method, focal mechanisms and location data for earthquakes and aftershocks originating nearby since 1966, geomorphic analysis based on newly acquired LiDAR data, and geological fieldwork were used to search for the DVF. We found small 10 cm wide vertical faults with horizontal shear striae on the drought-exposed shoreface of the reservoir within ~50 m of the upstream side of the dam, on both the north and south sides.

TABLE OF CONTENTS

LIST OF FIGURES

LIST OF TABLES

ACKNOWLEDGMENTS

I thank my wonderful wife Alicia for her daily support through every portion of this thesis. She more than anyone else, counselled with me, inspired me, and encouraged me as I worked on campus, at home, and in the field.

I also thank Dr. Vince Cronin for his patience, guidance, and unwavering commitment to my success.

I thank the Dallas Geological Society, Ellis Exploration, and the Baylor Geoscience Department for their financial support of this research.

CHAPTER ONE

Introduction

Dog Valley Fault

On September 12, 1966 at 8:31 A.M., an area near Truckee, California, was shaken by a M6.0 earthquake — the largest earthquake ever recorded in this area (Figure 1). People reported feeling the earthquake from San Francisco to Salt Lake City (Kachadoorian et al., 1967). Our best current estimate of the focal location of this earthquake is latitude 39.438°N and longitude 120.160°W at ~10 km depth (Ryall et al., 1968). Between September 12 and 25, 173 aftershocks were recorded using a local grid of seismographs (Greensfelder, 1968). Boca and Prosser Creek Dams were damaged along with bridges along Interstate Highway 80, the Union Pacific railroad corridor, and many structures in the greater Truckee area.

The Dog Valley Fault (DVF) is defined as the fault that produced the 1966 Truckee earthquake (Figure 2). The DVF is inferred to extend through Dog Valley northwest of Truckee, and is thought to have been responsible for a similar magnitude earthquake in 1948. Reuben Kachadoorian, Bob Yerkes, and A.O. Waananen of the USGS conducted three days of fieldwork in the epicentral area, beginning late on the day after the main earthquake. They wrote "Alignment of the zone of ground breakage with the trend of the fault exposed at Stampede damsite ... suggests an association with the fault; however, a thin veneer of undisturbed soil overlying the fault trace indicates that movement did not occur here during the earthquake" (Kachadoorian et al., 1967, p. 4). Several attempts were made to locate the DVF after the Truckee earthquake of 1966 (e.g., Kachadoorian et al., 1967; Hawkins et al., 1986); however, its ground-surface trace has not yet been located.

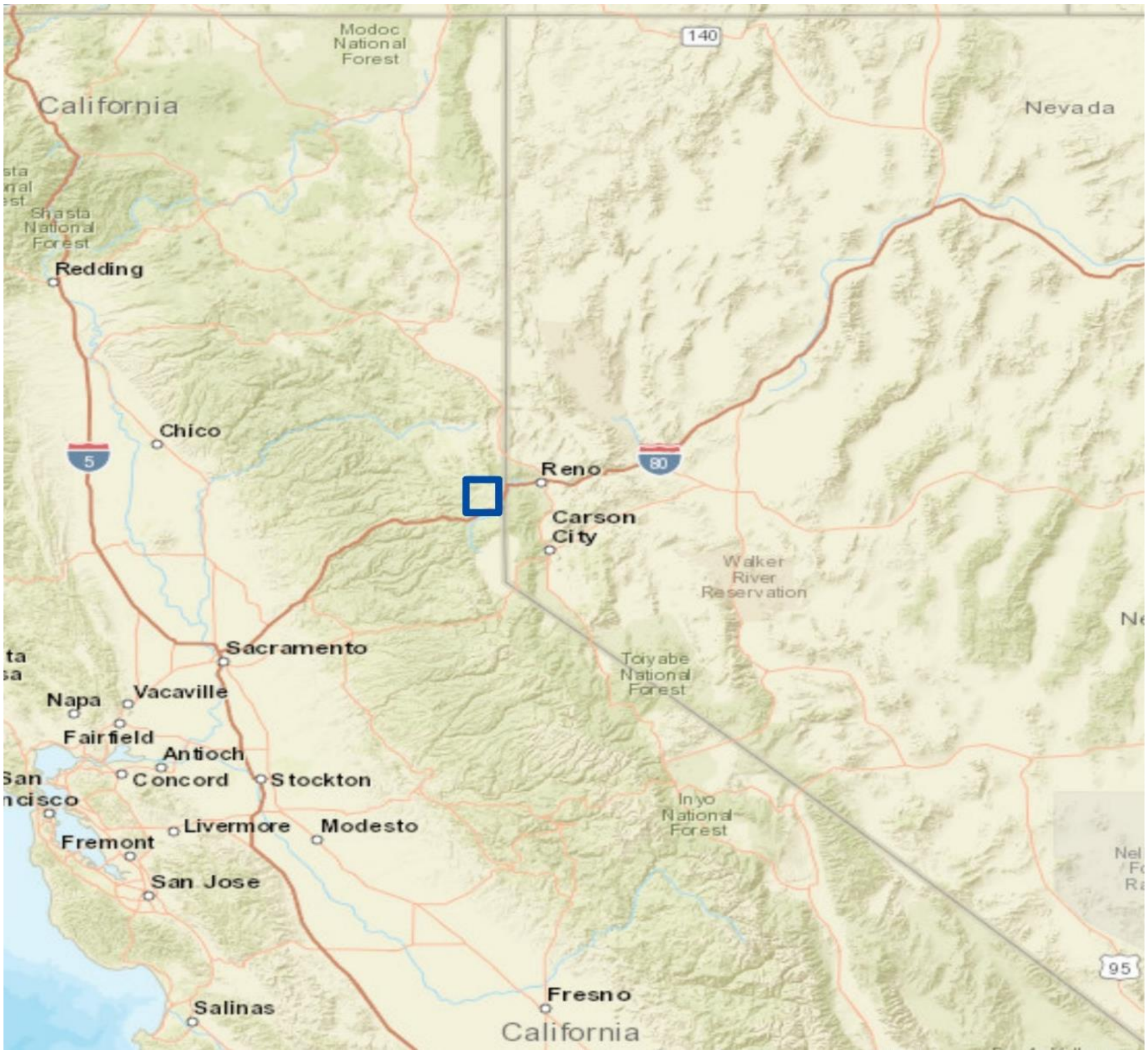

Figure 1. Location map. The blue box shows the study area for this thesis. This box is bounded by latitudes 39.370° to 39.544°, longitudes -120.211 to -120.037. Base map is from ESRI.

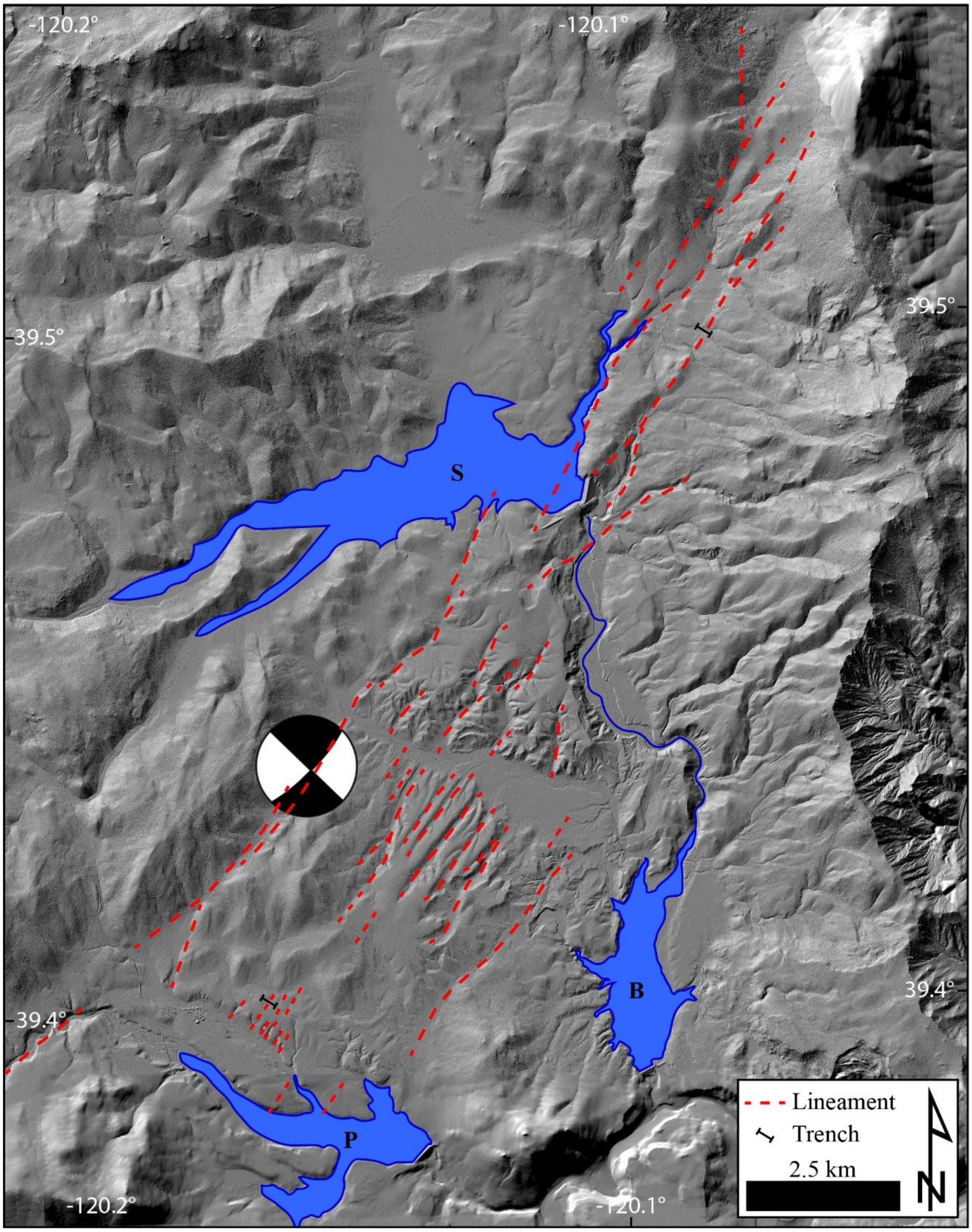

Figure 2. Study area bounded by latitudes 39.370° to 39.544°, longitudes -120.211° to -120.037°. The red curves are lineaments associated with the DVF (Hawkins et al., 1986; Olig et al., 2005). The focal mechanism diagram is drawn for the 1966 M6.0 Truckee earthquake. S is the Stampede Reservoir, P is the Prosser Creek Reservoir, and B is the Boca Reservoir.

Tectonic Setting

The Truckee–Lake Tahoe area is located within the transition zone between the Northern California Shear Zone and the northern Walker Lane (Figure 3). The Walker Lane is a zone of active right lateral shear between the Sierra Nevada Great Valley (SNGV) block and the western edge of the Basin and Range Province. The SNGV block

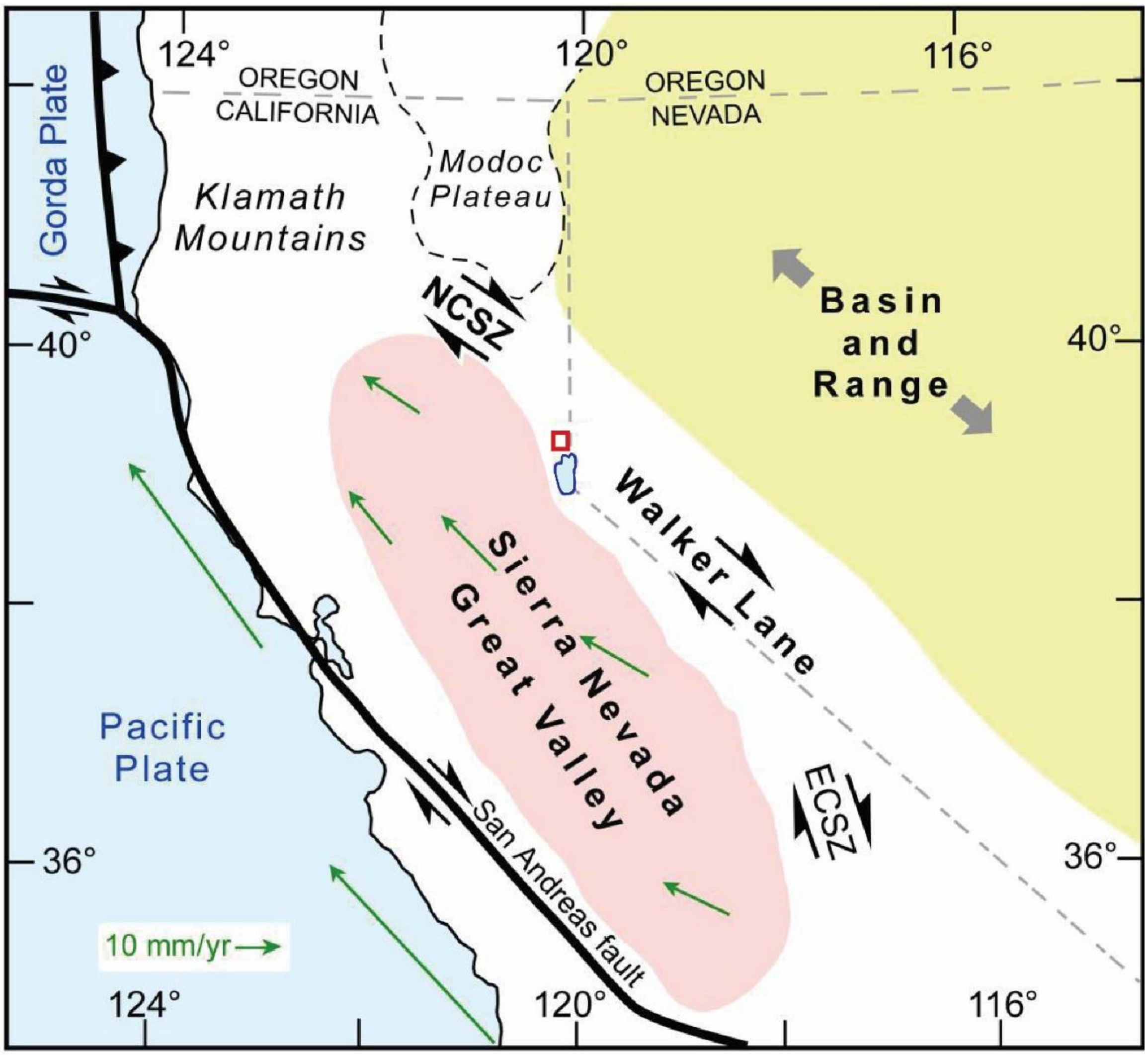

Figure 3. Tectonic setting. The study area is outlined by the red rectangle. ECSZ and NCSZ are the eastern California shear zone, and the northern California shear zone, respectively (Hammond et al., 2011). The green arrows show GPS velocities of various Plate Boundary Observatory sites relative to the Stable North American Reference Frame (Kreemer et al., 2003). Modified from Lindsay (2011).

moves steadily to the northwest at ~11-14 mm/yr relative to the stable cratonic interior of North America (Argus and Gordon, 1991; Dixon et al., 2000), approximately parallel to the motion of the Pacific plate. To the west of the SNGV beyond the San Andreas Fault, the Pacific Plate moves steadily to the northwest at roughly 3 times the velocity of the SNGV block, relative to cratonic North America (UNAVCO, 2017). The Walker Lane is thought to accommodate roughly 25% of the velocity between the Pacific and the North American plates (Argus and Gordon, 1991). Deformation within the northern Walker Lane is accommodated by a complex interplay of sinistral and dextral strike-slip faults, clockwise rotation, and some normal and oblique faults (Kreemer et al., 2009; Schweickert et al., 2004). The DVF is a left-lateral strike-slip fault within this deformation zone.

Prior Work

Roger Greensfelder, Reuben Kachadoorian, Bob Yerkes and A.O. Waananen of the USGS began working on the Truckee earthquake and the search for the DVF very soon after the main earthquake occurred on September 12, 1966. Kachadoorian, Yerkes, and Waananen worked to document damage and deformation associated with the earthquake, and sought to find evidence of surface faulting. They focused on a line of ground disturbance related to the earthquake that extended from Prosser Creek Reservoir northeast through the Stampede damsite toward Hoke Valley, along an azimuth of ~26° (Kachadoorian et al., 1967, Fig. 2). Greensfelder and members of the Stanford Research Institute installed several portable seismographs in the epicentral area and began recording aftershocks on September 14 (Greensfelder, 1968), ultimately adding 158 events in addition to 12 earlier events reported by the US Coast and Geodetic Survey.

Alan Ryall, J.D. VanWormer, and Austin Jones of the University of Nevada–Reno analyzed records from various permanent and temporary seismographs in the area to determine the focus and focal mechanism of the main earthquake as well as 108 epicenters and 79 focal depths for a set of aftershocks (Ryall et al., 1968). They noted that a 3-seismograph array in the epicentral area recorded more than 7800 aftershocks with magnitudes as small as 0.3 between September 14 and 29. Yi-Ben Tsai and Kehti Aki of MIT later used additional data to revise the focal mechanism solution for the main earthquake (Tsai and Aki, 1970).

Earthquakes that have occurred in this area since 1966 are also of interest, because some might be late aftershocks of the Truckee earthquake, independent events, or even foreshocks of a future large earthquake. Some of these more recent and better-located earthquakes might have occurred along the DVF. Focal locations for earthquakes in northern California and parts of adjacent states are relocated in a routine double-difference process described by Waldhauser (2009, 2017; Waldhauser and Schaff, 2008), and these relocated foci are broadly considered to be more reliable than the original focal locations computed using just the seismic records from individual earthquakes. Seismologists of the Northern California Earthquake Data Center have recomputed focal mechanisms by correcting data errors and incorporating data from additional networks to systematically revise and improve the focal mechanisms in their catalog (NCEDC, 2017).

Hawkins et al. (1986) conducted a seismotectonic study of the Truckee–Lake Tahoe area in support of the US Bureau of Reclamations system of dams and reservoirs. They suggested the DVF might extend from Prosser Creek Reservoir through Stampede Reservoir and Hoke Valley to Dog Valley. They excavated two trenches along what they had interpreted to be the probable trace of the active DVF — one near Prosser Creek Reservoir and the other on the southeast side of Hoke Valley — and did not encounter the fault in either trench (Figure 2). The ground-surface trace of the DVF has remained elusive.

Vince Cronin has developed the Seismo-Lineament Analysis Method or SLAM as a reconnaissance tool to correlate earthquakes with the ground-surface trace of the faults that generated them (e.g., Cronin et al., 2008; Cronin, 2014). He began work in the Tahoe area of California and Nevada in connection with an invited presentation at the 2009 annual meeting of the Association of Environmental and Engineering Geology held at South Lake Tahoe. Several students have continued that work.

Ryan Lindsay (2011) applied an early version of the SLAM code using data for 29 M≥3 earthquakes in the north Tahoe – Truckee area, broadly trying to correlate those earthquakes with known faults. Lindsay was able to spatially correlated earthquakes with the Dog Valley Fault Zone, the Polaris Fault, West Tahoe Fault, North Tahoe Fault, Incline Village Fault, and Agate Bay Fault (Lindsay, 2011).

Tyler Reed (2014) performed a similar analysis using an enhanced version of the SLAM code, focusing on the Polaris Fault, the Dog Valley Fault Zone, and two trends with no previously mapped faults that had been described by Lindsay (2011) — the Martis Creek trend, and the Prosser Creek trend. Reed (2014) considered 29 earthquakes, 26 of which were also used by Lindsay (2011). While his work yielded interesting results, Reed only had access to a relatively low-resolution digital elevation model (DEM) and corresponding hillshade map, which limited his geomorphic analysis. He also encountered private property restrictions in some key field sites along the Martis Creek and eastern Prosser Creek trends.

Jeremy Ashburn (2015) searched for evidence of the DVF in the research project for his bachelor's thesis, focusing on the north abutment of the Stampede Dam. Ashburn collected location and orientation data for several faults exposed in a roadcut on the north abutment of the Stampede Dam. His fieldwork in 2015 occurred during a major drought in which the level of the Stampede Reservoir was quite low, permitting examination of clean bedrock along the exposed shoreface around the margins of the reservoir.

Importance of Better Locating the Dog Valley Fault

The site of Stampede Dam had been chosen prior to the Truckee earthquake, and hence before the existence and seismogenic character of the DVF was known. Kachadoorian et al. (1967) noted that the Stampede damsite was located along the likely trace of the DVF, which produced the M6 earthquake. The epicenter of the Truckee earthquake is ~5 km southwest of the damsite (Figure 2). Stampede Dam was completed in 1970, four years after the Truckee earthquake and on the same site chosen before the earthquake. Stampede Reservoir is along the Little Truckee River north of Boca Reservoir. Nearby Prosser Creek Reservoir is along or adjacent to the inferred trend of the DVF, ~8 km south of Stampede Reservoir on a different tributary of the Truckee River.

The current estimated location of the DVF is under or adjacent to the Stampede Dam (USGS, 2017; Hawkins et al., 1986; Kachadoorian et al., 1967). A seismic safety report prepared for the City of Truckee by Early et al. (2006) estimates that the maximum credible earthquake that can be produced by the DVF is a M6.75 event. Slip on the DVF associated with an earthquake of similar magnitude to the 1966 Truckee earthquake, but with a more shallow focal depth, might result in seismically induced failure of the Stampede Dam.

A US Bureau of Reclamation (USBR) study completed in 2004 "concluded that Stampede Dam does not meet Reclamation dam safety guidelines for both hydrologic and seismic failure modes..." (referenced in Schmidt et al., 2012, p. 1-6). A construction project is currently in progress that will increase the height of Stampede Dam by 3.5 m through the construction of a mechanically stabilized earth (MSE) structure along the crest of the dam, directly above the dam core. The MSE is contained between concrete slabs, and the entire 9.1 m wide 3.5 m tall wall is designed to enable the dam to contain the 250,000-year "probable maximum flood."

The USBR modeled the consequences of a Stampede Dam failure in a subsequent Safety of Dams report and determined that if the earth-fill Stampede Dam fails, the Stampede Reservoir would flood down the Little Truckee River and into the Boca Reservoir (Schmidt et al., 2012). The influx of water into the Boca Reservoir would result in uncontrolled flow over the Boca Dam, which is another earth-fill structure. The Boca Dam would fail as its crest erodes and its core is exposed, and the combined volume of the two reservoirs would flow down the Truckee River Gorge. The volume of water stored in these two reservoirs is typically ~200,000 acre-feet of water and could be as high as 300,000 acre-feet (DWR, 2017).

The Truckee River Gorge drops ~330 m in elevation over a distance of ~47 km along the channel from the Boca Dam to downtown Reno, Nevada. As the Truckee River approaches Reno, the Truckee River Gorge transitions into the Truckee River floodplain.

The USBR reported 148,400 people reside within the boundaries of the would-be disaster area indicating an enormous likely loss of life and property resulting from a Stampede Dam failure (Schmidt et al., 2012). Additionally, a daily average of 45,000 tourists stay in various hotels, resorts and casinos in Reno and Sparks, Nevada, the majority of which lie within the potential disaster area along the Truckee River (InfoSearch International, 2006).

The same USBR report that proposed modifications of Stampede Dam to mitigate the risk of dam failure due to overtopping during a "maximum probable flood" summarily dismissed potential earthquake risks without explicit consideration of the DVF, stating "the possibility of a seismic induced failure is extremely remote" (Schmidt et al., 2012, p. 1-7). On its face, it seems remarkable that seismic risk is not discussed thoroughly in any such plan, particularly with knowledge that the DVF has produced a M6 earthquake within living memory. Lack of a confirmed ground-surface trace for the DVF or its formal recognition as an active seismogenic fault probably contributes to the underestimation of its hazard potential.

Purpose of this Research Project

The purpose of this research project is to use the Seismo-Lineament Analysis Method and the best relevant seismic, topographic, and geodetic data currently available to better constrain the ground surface trace of the Dog Valley Fault. The hazard potential of the DVF will not be fully considered in regional seismic risk assessments until the DVF is better located and characterized. The study area is from latitude 39.370°N to 39.544°N, and from longitude 120.211°W to 120.037°W.

The current version of the SLAM code was used, along with the current best focal locations from the catalog maintained by Waldhauser (2017), the revised focal mechanisms in the Northern California Earthquake Data Center mechanism catalog (NCEDC, 2017; Tsai and Aki, 1970), and the standard USGS 9-m resolution DEM of the study area (USGS, 2016). Geomorphic analysis was performed using hillshade maps created in ArcGIS from 1-m resolution bare-earth DEMs derived from recent aerial LiDAR surveys of the area (USACE, 2008; NCALM, 2014). Fieldwork in September 2016 took advantage of near-historic low water levels in Stampede and Prosser Creek Reservoirs, which allowed examination of clean exposures along the upper shoreface of those basins. Crustal strain rates computed from GPS velocity data are used to assess horizontal infinitesimal strain across the study area (UNAVCO, 2017; Nevada Geodetic Laboratory, 2017).

CHAPTER TWO

Methods and Primary Data

SLAM

The Seismo-Lineament Analysis Method or SLAM has been developed by Cronin to utilize data from well-located earthquakes and their focal mechanism solutions to constrain where a geologist would look to find the zone along which the active fault is most likely to be found at the ground surface (Cronin et al., 2008; Cronin, 2014). That zone is called a seismo-lineament (Figure 4).

SLAM includes several steps. The first step is to project the two nodal planes from the earthquake focus to the ground surface, plus-or-minus the relevant uncertainties, to establish the boundaries of the seismo-lineament where the fault is likely to be found. The *Mathematica* code that performs this task requires as input the latitude, longitude, and depth of the earthquake focus, the strike (or dip direction) and dip angle of the nodal planes, and a suitable digital elevation model (DEM) of the ground surface in the epicentral area. The output of the SLAM code is a map of the boundaries of the seismo-lineament superimposed on the hillshade map. The details of the process of defining the boundaries of a seismo-lineament are described elsewhere (e.g., Cronin et al., 2008; Cronin, 2014; Worrell, 2014).

The second step in SLAM is to conduct a geomorphic analysis using the highest-resolution bare-earth hillshade map of the study area that is available. In this research project, LiDAR data were available so that the DEM and resulting hillshade maps had a

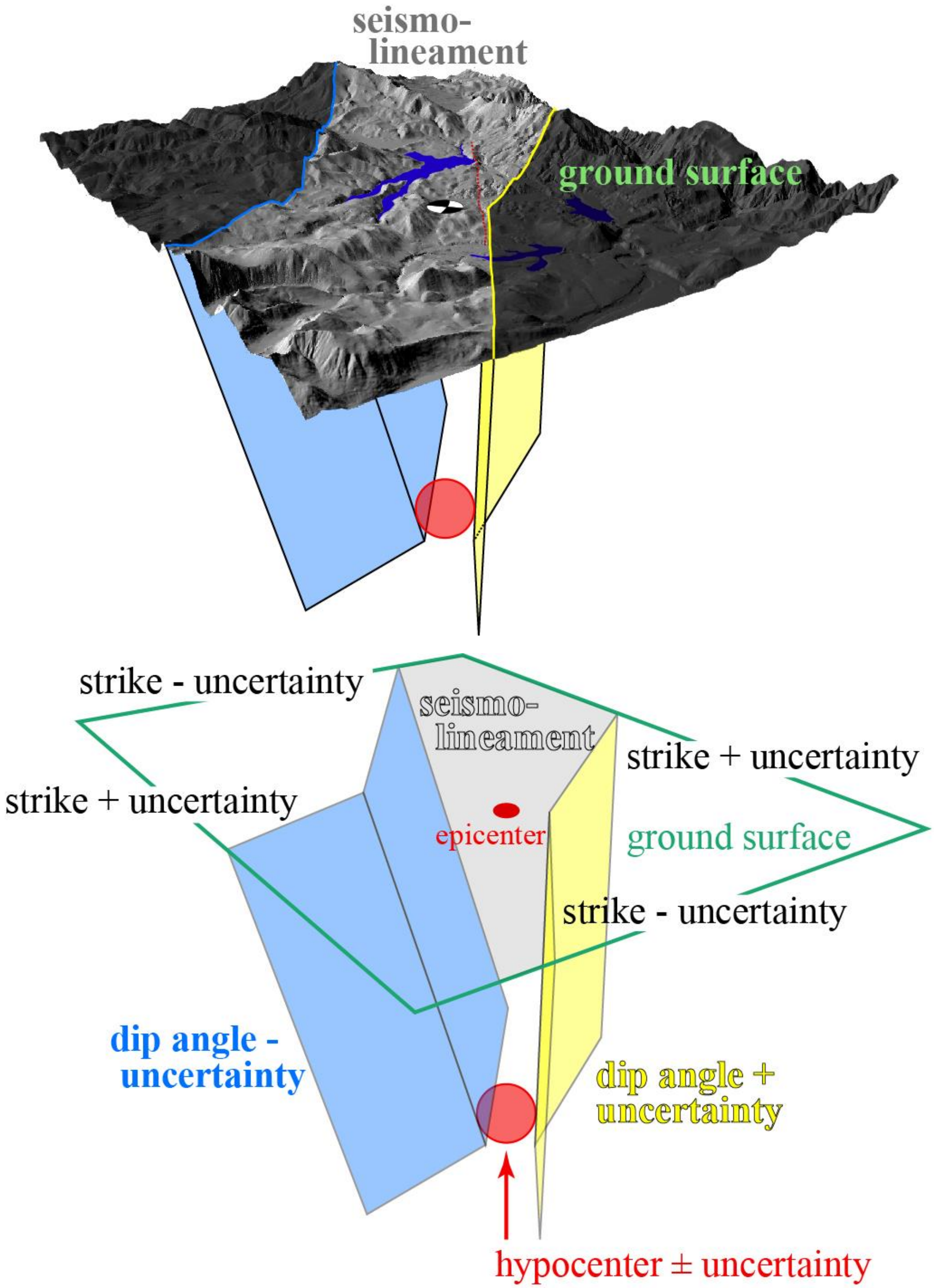

Figure 4. Geometry of a seismo-lineament. The seismo-lineament is defined as the area between the planes inclined at the dip angle minus uncertainty (blue) and dip angle plus uncertainty (yellow) plus and minus the strike uncertainty. This example is based on earthquake S1, the 1966 M6.0 Truckee earthquake. After Reed, 2013.

horizontal resolution of ~1 m. It is the area within a given seismo-lineament that is the focus of the geomorphic analysis. The hillshade map is illumined at a low elevation relative to horizontal, in a direction that is perpendicular to the strike of the nodal plane (or the inferred fault trend) in order to accentuate geomorphic features that might be associated with faulting. Geomorphic lineaments that might represent fault traces are mapped, and these are the equivalent of fault-location hypotheses that can be tested during subsequent field work.

The third step in SLAM is to conduct fieldwork in the study area, seeking to find evidence of faulting within the area bounded within the seismo-lineament. In particular, the trends defined by geomorphic lineaments that are within and spatially compatible with a given seismo-lineament are surveyed for evidence of faulting. A fault is considered to be spatially correlated with an earthquake nodal plane if the fault has the following geometric characteristics: its location is within the corresponding seismo-lineament; its orientation is within the uncertainty region of the corresponding nodal plane; and the orientation of its slip vector is within the uncertainty region around the slip vector on the nodal plane. Fisher statistics are typically used to describe the mean and variation around the mean for vector data used in fault analysis (Fisher, 1953; Cronin, 2008). A convincing spatial correlation should also be supported by evidence of low-PT deformation mechanisms along the fault, such as the development of a fault core that contains breccia or clay gouge.

Earthquake Locations

Felix Waldhauser uses a double-difference method to relocate earthquakes that occurred in northern California and adjacent parts of surrounding states (Waldhauser, 2008; Waldhauser and Schaff, 2008). His online catalog includes 382 earthquakes with epicenters located within the study area of this project and that have occurred between the beginning of 1984 and June 2017 (Figure 5; Waldhauser, 2017). Each focal location in his catalog includes the latitude, longitude, depth, and uncertainty estimates in three orthogonal directions — two horizontal directions and vertical. The uncertainty volume around the mean focal location is an ellipsoid, and the current SLAM code is written to accommodate this geometry.

The origin time and focal location data for the 11 earthquakes examined in this research project are presented in Table 1. Each of these earthquakes have epicenters located within the study area and have focal mechanism solutions that have either been published in the literature (Tsai and Aki, 1970; Ryall et al., 1968) or posted via the NCEDC mechanism catalog (NCEDC, 2017). The focal location for the Truckee earthquake (labeled S1 in Table 1) is from Ryall et al. (1968), who did not publish uncertainties for the location. An uncertainty of 2 km for all axes was assumed for this event. The focal locations for the other two earthquakes in Table 1 that occurred prior to 1984 (S2 and S3) were taken from the NCEDC mechanism catalog (NCEDC, 2017), and all focal locations from 1984 to the present were from Waldhauser's relocated earthquake catalog (Waldhauser, 2017).

The vertical uncertainty posted in Waldhauser's catalog was zero in several cases, while the corresponding horizontal uncertainties were non-zero. The depth of an earthquake focus is usually the most poorly constrained location parameter, so it did not make physical sense to have zero uncertainty along the vertical axis. The SLAM code would not be able to handle a focal uncertainty volume that had no vertical extent. To resolve this problem, the initial vertical uncertainty value was replaced with the maximum horizontal uncertainty value plus 0.001 km in cases where the vertical uncertainty was originally listed as zero (S4, S5, S9, S10, S11, S12, S13, and S14).

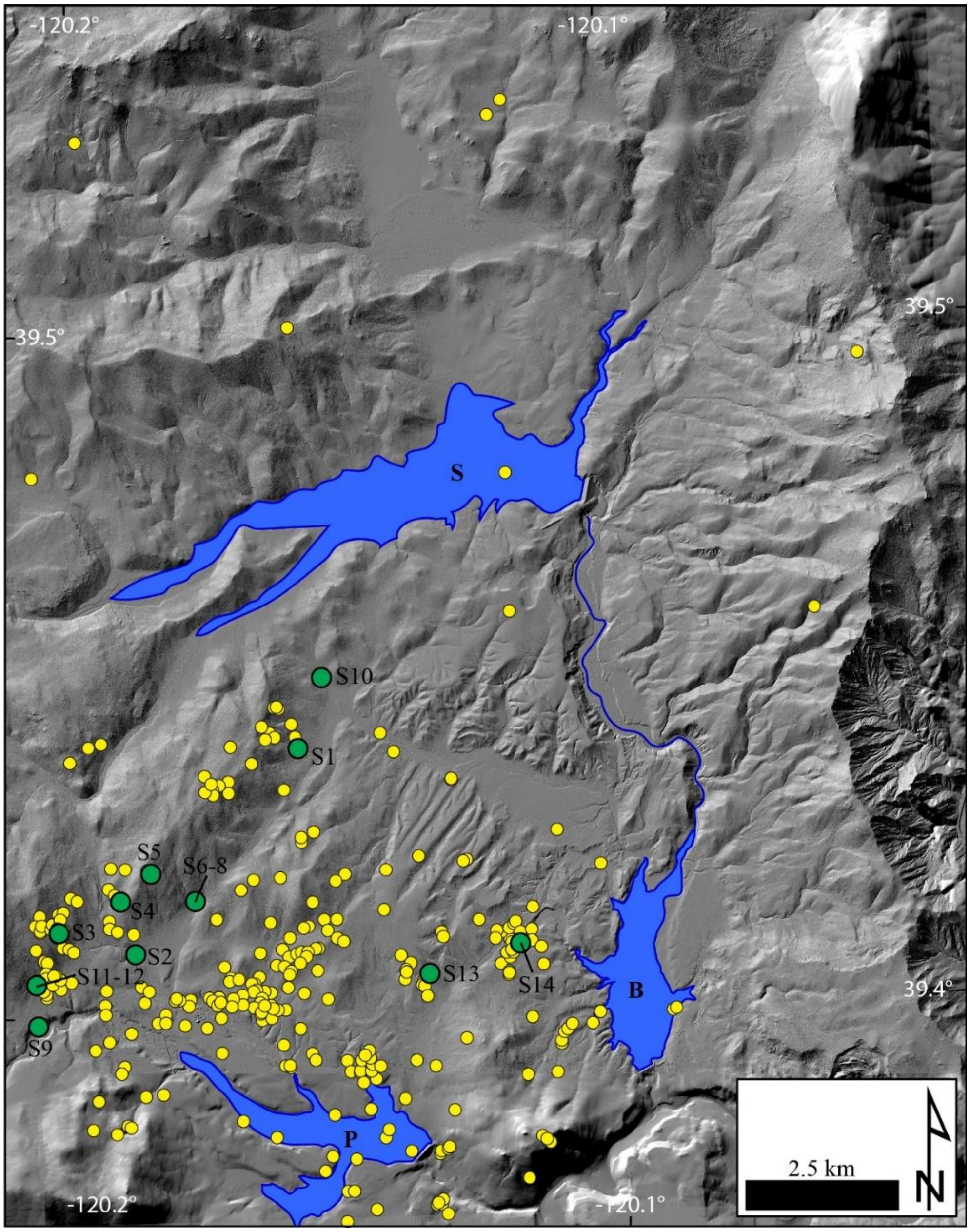

Figure 5. Locations of earthquake epicenters. Yellow circles mark epicenters for all earthquakes in the study area from 1984 through May 2017 that were relocated by Waldhauser (2017). Green circles mark epicenters of earthquakes S1-S14 with published/posted focal mechanisms studied in this project.

Table 1. Origin time and location of earthquakes used in this study.

Local ID	Year	Mo	Da	Hr	Min	Sec	Lat	Long	Depth (km)	Horiz Error 1	Horiz Error 2	Eh1 Azimuth	Vert Error
S1	1966	9	12	16	41	0	39.438	-120.16	10	2	2	1	2
S2	1977	1	11	8	50	6.97	39.4087	-120.1918	8.3	0.5	0.5	1	0.6
S3	1983	7	3	15	8	19.49	39.4122	-120.2063	8.73	0.3	0.3	1	0.8
S4	1985	5	4	15	56	37.86	39.41656	-120.1946	10.391	0.024	0.017	37	0.025
S5	1992	8	30	23	42	8.34	39.42047	-120.18852	5.344	0.539	0.026	64	0.54
S6	1993	8	6	0	31	38.45	39.41621	-120.18018	0.368	0.474	0.023	64	2
S7	1993	8	6	0	31	38.45	39.41621	-120.18018	0.368	0.474	0.023	64	2
S8	1993	8	6	0	31	38.45	39.41621	-120.18018	0.368	0.474	0.023	64	2
S9	1993	8	9	2	19	7.82	39.3988	-120.2107	9.27	1.3	1.3	1	1.301
S10	1998	1	15	15	12	14.58	39.4481	-120.15511	4.636	0.43	0.028	64	0.431
S11	2004	6	12	14	49	0	39.40479	-120.2107	7.292	0.032	0.021	74	0.033
S12	2004	6	12	14	49	0	39.40479	-120.2107	7.292	0.032	0.021	74	0.033
S13	2011	11	22	18	23	26.07	39.40473	-120.13639	10.139	0.023	0.019	67	0.024
S14	2011	12	23	5	30	29.85	39.40871	-120.11916	0.882	0.026	0.02	82	0.027

Epicenter of S1 from Ryall et al. (1968), with estimated uncertainties. Epicenters of S2-S3 from Northern California Earthquake Data Center Mechanism Catalog (1968 - Present), accessible via http://www.quake.geo.berkeley.edu/ncedc/catalog-search.html. Relocated epicenters (S4-S14) from Waldhauser (2017) accessible via http://ddrt.ldeo.columbia.edu/DDRT/index.html

Earthquake Focal Mechanisms

Earthquake focal mechanism solutions for most earthquakes used in this research were computed using FPFIT (Reasenberg and Oppenheimer, 1985) and are accessed through the Northern California Earthquake Data Center (NCEDC, 2017). The focal mechanism of the 1966 Truckee earthquake is by Tsai and Aki (1970). They did not report orientation uncertainties for the nodal planes, so 10° uncertainties in dip direction, dip angle, and rake were assumed. Two of the eleven earthquakes in this research area have multiple focal mechanism solutions posted in the NCEDC mechanism catalog, so a total of fourteen focal mechanisms were available for SLAM analysis (Table 2).

Focal mechanism diagrams were created in a Wolfram Demonstration Project application titled Earthquake Focal Mechanism (Scherbaum et al., 2013). This application was also used to determine the second nodal planes of the earthquake focal mechanism solutions. Focal mechanism diagrams were plotted as equal area, lower hemisphere projections and exported into Adobe Illustrator CC 2015 for use in associated figures.

Table 2. Magnitude and fault plane solution of earthquakes used in this study.

Local ID	Earthquake Magnitude	Dip Trend	Dip Angle	Rake Angle	Dip trend 90% CI	Dip angle 90% CI	Rake 90% CI
S1	6	134	80	0	10	10	10
S2	2.97	120	65	-10	20	43	50
S3	4	300	80	20	8	13	30
S4	2.7	125	54	-31	15	40	35
S5	3.2	301	61	12	15	25	25
S6	3.1	333	48	59	18	13	40
S7	3.1	115	50	-70	13	3	5
S8	3.1	325	90	30	23	28	10
S9	3	319	33	28	20	23	25
S10	3.8	290	35	30	10	23	10
S11	3.7	145	75	-20	8	40	35
S12	3.7	319	63	-53	8	10	15
S13	2.7	125	80	-20	8	30	20
S14	3	145	80	0	10	33	30

Focal mechanism of S1 from Tsai and Aki (1970), with estimated uncertainties. Focal mechanisms of S2-S14 from Northern California Earthquake Data Center Mechanism Catalog (1968 - Present), accessible via http://www.quake.geo.berkeley.edu/ncedc/catalog-search.html. Second nodal planes determined using http://demonstrations.wolfram.com/EarthquakeFocalMechanism/

Digital Elevation Models and Hillshade Maps

The SLAM code uses a lower-resolution digital elevation model (DEM) provided by the USGS (USGS, 2016). The low resolution results in a smaller data file, and decreases the time needed to find the position of the seismo-lineament boundaries across the digital topography. This DEM is a simple ASCII file with six lines of header information preceding a rectangular matrix of elevation data composed of hundreds or thousands of rows and columns of elevations. The horizontal location of each elevation datum is computed by knowing the grid spacing (typically ~9 meters) and the number of rows and columns from a corner of the matrix whose UTM coordinates are known. The header information includes the number of rows and columns in the matrix, the UTM coordinates of the lower left corner of the matrix, the grid or cell spacing, and the value to be interpreted as a null value. The SLAM code creates a hillshade map, plots the epicenter, and drapes the seismo-lineament boundaries across the map.

All of the previous SLAM studies worked only with the standard 9-m DEMs that are freely available from USGS (USGS, 2016). Aerial LiDAR missions have been flown in the Tahoe-Truckee area in recent years in support of public planning, watershed modeling, and fault reconnaissance. We gained access to two aerial LiDAR datasets that are relevant to this research project.

The first dataset comes from a mission flown in September 2008 in an attempt to map the ground surface trace of the Polaris Fault, and covers the southern portion of the DVF study area (USACE, 2008; Hunter et al., 2011). These LiDAR data were downloaded as 157 raster tiles from the Geospatial Repository and Data Management System (GRiD) site developed and maintained by the US Army Corps of Engineers. The tiles were merged into one large DEM using the "Mosaic to New Raster" tool in ESRI ArcGIS. The process is as follows. First, all 157 rasters were loaded into the "Input Raster" field. The output raster was then named and its output location specified. Because these input rasters are georeferenced, the "Spatial Reference" category was left alone. The "Mosaic Operator" defines how ArcGIS handles raster overlap. "Mean" and "Blend" approximated a seamless mosaic better than any other options and were therefore chosen as the mosaic operators. This near seamless mosaic DEM was then analyzed in ERDAS in order to classify returns and create a bare-earth DEM. The resultant bare-earth DEM has a 2-meter resolution.

The second aerial LiDAR dataset was collected by the National Center for Airborne Laser Mapping (NCALM, 2014). This mission was flown in 2013 and 2014 over the greater Truckee area. A 1-meter horizontal resolution bare earth DEM was included in the LiDAR data package. The classification of ground points for this DEM was done through an automated process using TerraScan 14.020. The vertical datum for these data is NAVD88, Geoid 12a. The horizontal datum is NAD83, 2011. The projection is UTM Zone 10N.

Structural-Geomorphic Analysis

ArcGIS 10.4.1 software was used to create improved hillshade images and analyze these hillshades for geomorphic indicators of faulting (Table 3). Improved hillshade images were rendered with illumination at low sun angles perpendicular to the fault trend. A total of six such hillshade images were created. The improved hillshades were illuminated from either side of the fault trend at 135° and 315°, with sun angles at 15°, 30°, and 45° above the horizon. By doing this, the topographic deviations parallel to the DVF are accentuated. Hunter et al. (2011) used similar methods to identify and constrain geomorphology related to the active Polaris Fault — a newly discovered dextral strike slip fault just north of Truckee, CA.

Table 3. Geomorphic Indicators of Faulting.

Stream Channels that are aligned on opposite sides of a drainage divide
Lower-order stream channel aligned across a higher-order stream channel
An anomalously straight segment of a stream channel
Aligned straight segments of one or more stream channels
Lower-order stream channels whose trend is directed upstream relative to the higher-order stream it intersects, so that water flowing from the smaller stream into the larger stream must change directions at an obtuse angle
Abrupt changes in gradient across a stream channel
A stream channel that steps down in the direction of flow, indicated by a nickpoint (i.e. rapids, waterfall)
A stream channel that steps up in the direction of flow, indicated by a pool
Apparent lateral deflection of an incised stream channel or floodplain
Abrupt changes in gradient along a ridge crest
A ridge that steps down abruptly in the direction of decreasing elevation
A ridge crest that steps up in the direction of decreasing elevation
A saddle in the ridge crest
Apparent lateral deflection of a ridge crest
Abrupt changes in the gradient of a surface localized along a narrow linear step (fault scarp)
Benches or faceted spurs at the base of ridges that are apparently unrelated to coastal or fluvial erosion
A set of ridges in an en echelon array
A topographic basin along a linear trough (pull-apart basin, sag pond)
A topographic hill along a linear trough (pop-up, pressure ridge)
A ridge across the mouth of a stream drainage that is not a glacial moraine (shutter ridge)

From Cronin et al., 2008, after Ray, 1960; Miller, 1961; Wesson et al., 1975; Bonilla, 1982; Slemmons and dePolo, 1986; Cronin et al., 1993; McCalpin, 2009; and Burbank and Anderson, 2001.

Fieldwork

Field studies were carried out in the study area September 21– 29, 2016. A variety of techniques were used to identify places on the landscape that might be affected by recent faulting.

Ground surface lineaments are key indicators of faulting and fracturing. Examples of ground surface lineaments include linear vegetation patterns such as a line of trees in an area dominated by underbrush or a linear boundary between two dominant types of vegetation. Vegetation health can also be used as a discriminator with the underlying assumption that plant life on one side of the fault receives superior nutrition than the other. Small linear topographic trends can indicate faulting, such as a laterally extensive step in a slope or a drainage way aligned sub-perpendicular to the slope. The same is true of linear topographic trends such as ridges or valleys, points or draws that might extend over long distances. A list of other such indicators that are large enough to be observable in aerial imagery is presented in Table 3.

Faults encountered in the field were photographed, located using a hand-held GPS receiver, and excavated to a minor extent where possible. Useful characteristics included the width of the fault core (if any) and the nature of the material within the core (e.g., breccia, gouge, dry/wet conditions, roots, burrows). If the boundary between the fault core and the damage zones adjacent to the core could be excavated, it was cleaned gently and examined for shear striae. If shear striae were present, their orientation was measured as evidence of the direction of the last slip event along the fault. The orientation of the fault surface was measured to determine strike and dip. All of these orientation indicators were measured several times — ideally, seven or more times at a site, so that reliable site means could be determined using Fisher statistics (Fisher, 1953; Cronin, 2008). Measurement uncertainties involved in using the Brunton Compass were assumed to be ±2°. The lateral extent of the fault was mapped as far as conditions allowed.

GPS Velocities

GPS velocity data from three non-colinear sites (i.e., from a triangle of 3 sites) was used to measure crustal strain in a horizontal plane. The GPS Triangle Strain Calculator prepared for UNAVCO by Cronin (2012) was used for horizontal strain calculations. The strain calculator uses as input the latitude, longitude, and orthogonal velocities in the north, east, and up directions plus associated velocity uncertainties. The results include the average translation rate, rotation rate, and distortion rate for the area bounded by the triangular array.

Eleven GPS stations with velocity data relevant to the DVF are used in this research. These stations are either part of the Plate Boundary Observatory (PBO) GPS network (UNAVCO, 2017) or the University of Nevada Reno's MAGNET GPS network (Nevada Geodetic Laboratory, 2017). The GPS velocities from these stations are measured relative to the North America-fixed reference frame NA12 (Blewitt et al. 2013). Figure 6 shows a map of these GPS stations and their spatial relation to the inferred trace of the DVF. The location and velocity data associated with these stations are listed in Table 4.

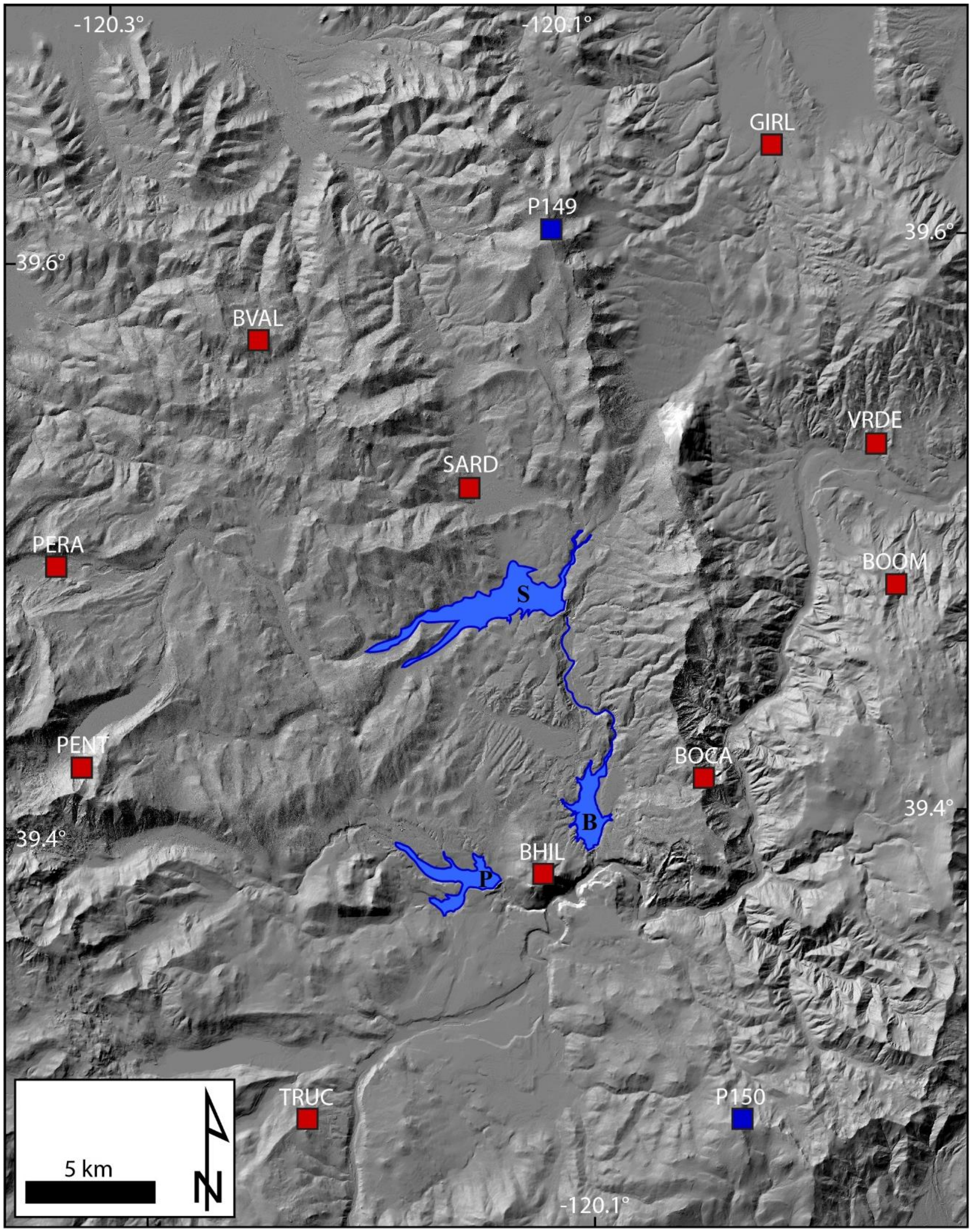

Figure 6. Spatial geometry of the eleven GPS stations used in the crustal strain analysis. GPS stations from the University of Nevada Reno's MAGNET network are shown as red squares. GPS stations from the Plate Boundary Observatory network are shown as blue squares.

Table 4. Locations and velocities for GPS stations used in this study.

4 character Station ID	Latitude	Longitude	East velocity	East velocity uncertainty	North velocity	North velocity uncertainty
BHIL	39.379	-120.118	-8.363	0.142	5.760	0.140
BOCA	39.411	-120.045	-8.159	0.232	5.282	0.258
BOOM	39.476	-119.956	-7.529	0.225	5.587	0.169
BVAL	39.565	-120.237	-8.310	0.360	5.367	0.382
P149	39.602	-120.105	-7.609	0.165	5.057	0.240
P150	39.292	-120.034	-8.506	0.191	5.788	0.161
PENT	39.419	-120.323	-9.305	0.458	6.557	0.438
PERA	39.488	-120.332	-8.968	1.147	6.572	0.633
SARD	39.513	-120.146	-8.152	0.400	5.532	0.405
TRUC	39.296	-120.228	-8.281	0.376	6.222	0.433
VRDE	39.524	-119.962	-7.838	0.432	4.484	0.599
GIRL	39.628	-120.005	-7.419	0.547	4.704	0.533

Velocity data from P149 and P150 are from the PBO network (UNAVCO, 2017). All other data are from the MAGNET network (Nevada Geodetic Laboratory, 2017). These data are inputs for the GPS Triangle Strain Calculator prepared for UNAVCO by Cronin (2012).

CHAPTER THREE

Results

SLAM

The seismo-lineament analysis was used to identify earthquakes that might have occurred along the same fault that generated the Truckee earthquake in 1966, and to aid in the location of the Dog Valley Fault. The usual process of using SLAM to spatially correlate an earthquake with a known fault is not applicable because we do not have accurate knowledge of where the ground-surface trace of the Dog Valley Fault is. In the absence of a very good location for the main shock or accurate knowledge of the ground-surface trace of the causative fault, the strategy is to try to spatially correlate the fault plane solution of the main shock with inferred fault plane solutions from more recent, better located earthquakes.

The raw output from the SLAM code was re-projected in ArcGIS 10.4.1 and exported into Adobe Illustrator CC 2015 to create the final graphics documents that include the seismo-lineaments and focal mechanism diagrams. Seismo-lineaments were drawn individually for S1, S2, S3, S5, S8, S11, S13, and S14 and are presented as the light gray areas bounded by darker gray areas that lie outside of the seismo-lineaments in Figures 7 - 14, respectively. The focal mechanism diagrams are lower-hemisphere equal-area projections. Each of these figures includes dashed red curves showing the location of geomorphic lineaments inferred to be related to the DVF (Hawkins et al, 1986) that have been assumed to be coincident with the DVF trace in the Quaternary Fault and Fold

Database of the United States (USGS, 2017). The actual location of the DVF is currently unknown.

The seismo-lineament for the 1966 Truckee earthquake is based on the focal location of Ryall et al. (1968) with assumed location uncertainties of 2 km and the focal mechanism solution of Tsai and Aki (1970) with assumed uncertainties of 10° in the dip direction, dip angle, and rake of the fault plane solution (Figure 7). The ground-surface trace of the DVF should be located within the light gray area in Figure 7. The Truckee earthquake resulted in left-lateral (sinistral) shear on a plane dipping ~80° to the southeast and striking ~44° (toward the northeast), so the trace of that fault is expected to be a rather straight line along most of its length that is little deflected by topography.

The seismo-lineament associated with event S2 (Figure 8) is very broad due to large uncertainties in the orientation of the fault plane solution, overlapping the S1 seismo-lineament. While this event might have occurred on the DVF, data associated with it are not helpful in resolving the location of the fault. The fault plane solution indicates oblique displacement with normal dip-slip and sinistral strike-slip components.

Event S3 was a M4 earthquake with sinistral shear on a steeply dipping plane. The fault plane solution has relatively small orientation uncertainties, so the seismo-lineament is relatively narrow (Figure 9). There is a significant overlap in the S1 and S3 seismo-lineaments.

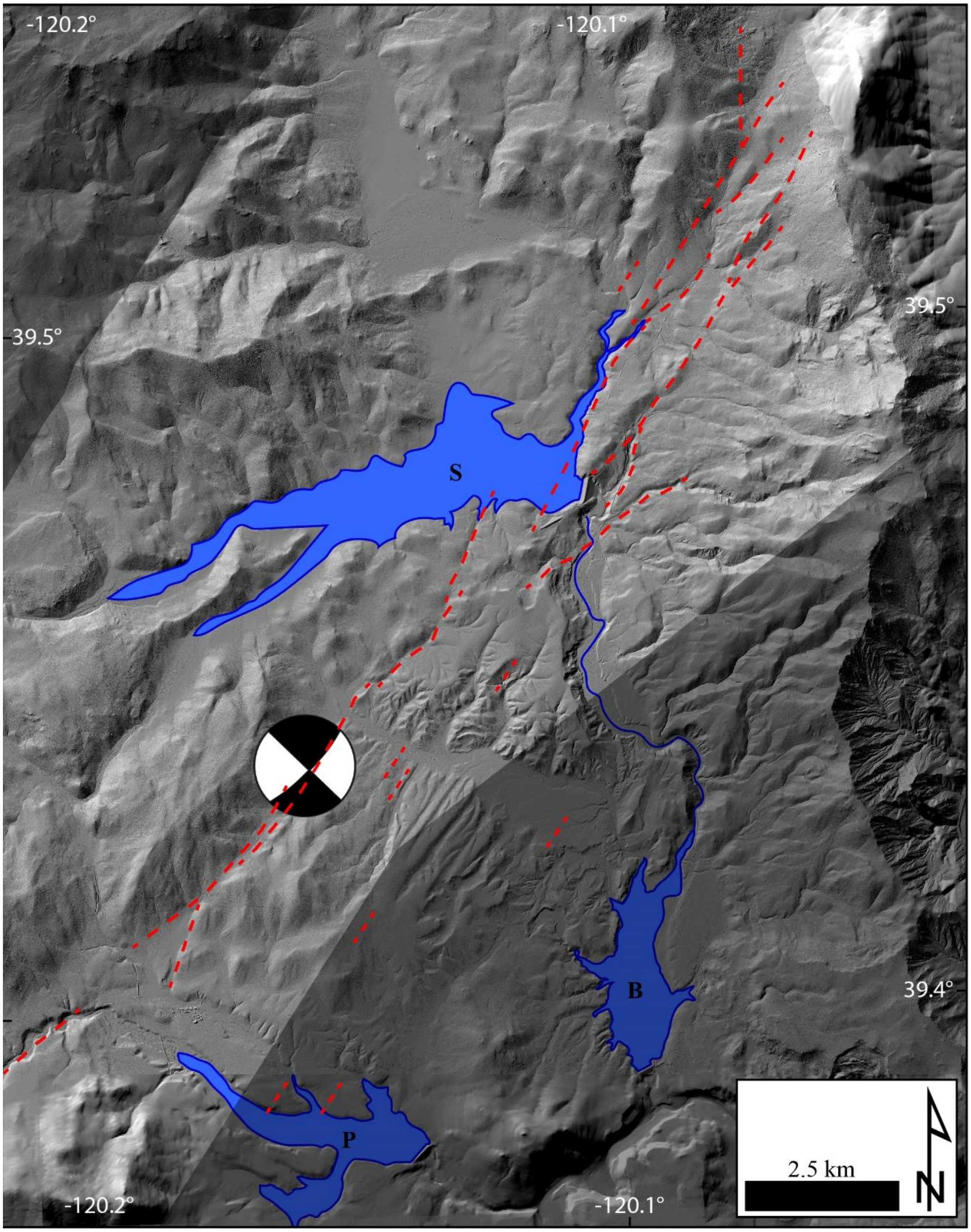

Figure 7. Hillshade image of the seismo-lineament for S1. This M6.0 earthquake occurred on 9/12/1966 at a depth of 10 km. The dashed red curves are geomorphic lineaments inferred to be related to the DVF (Hawkins, 1986, p. 66).

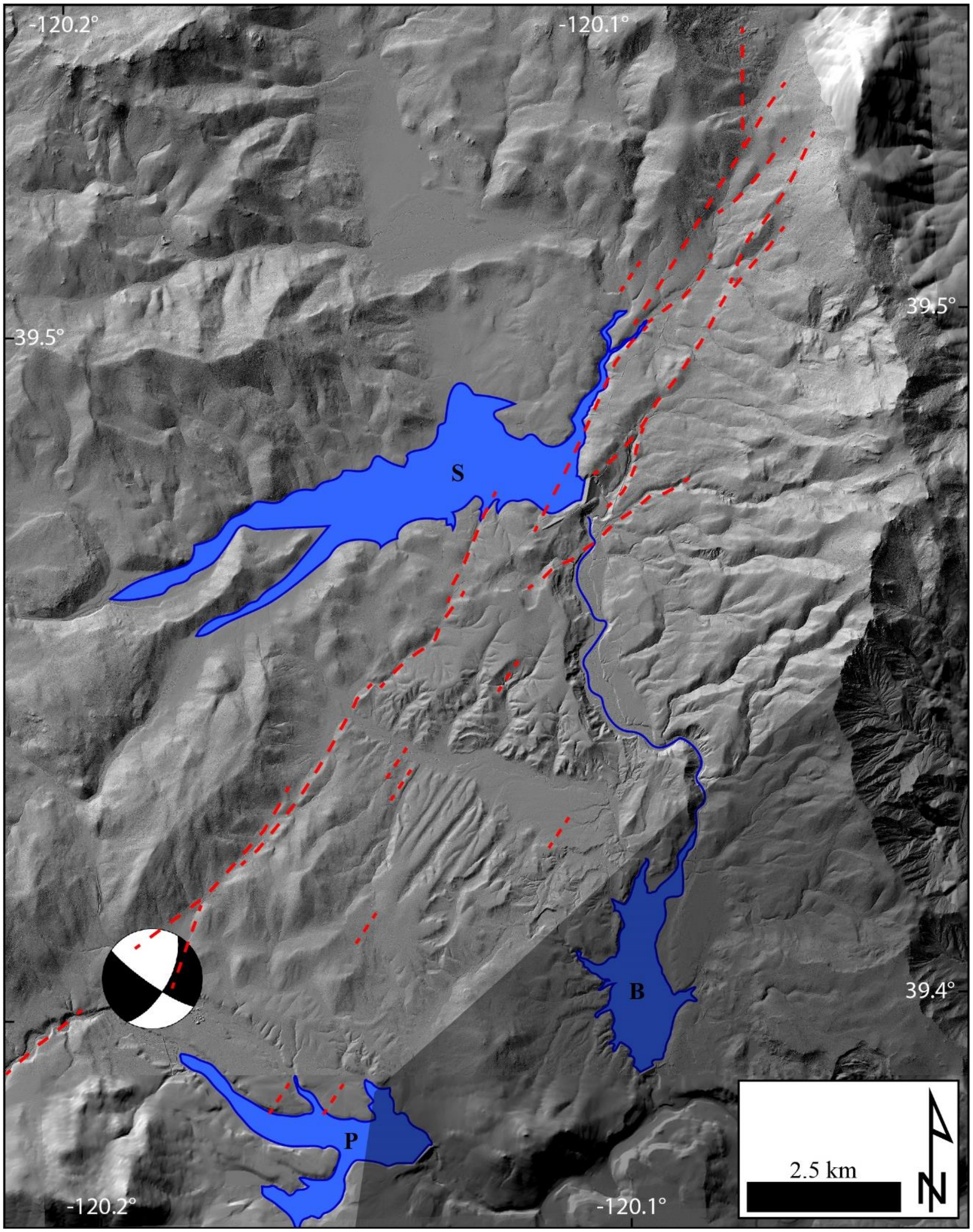

Figure 8. Hillshade image of the seismo-lineament for S2. This M2.97 earthquake occurred on 1/11/1977 at a depth of 8.3 km. The dashed red curves are geomorphic lineaments inferred to be related to the DVF (Hawkins, 1986, p. 66).

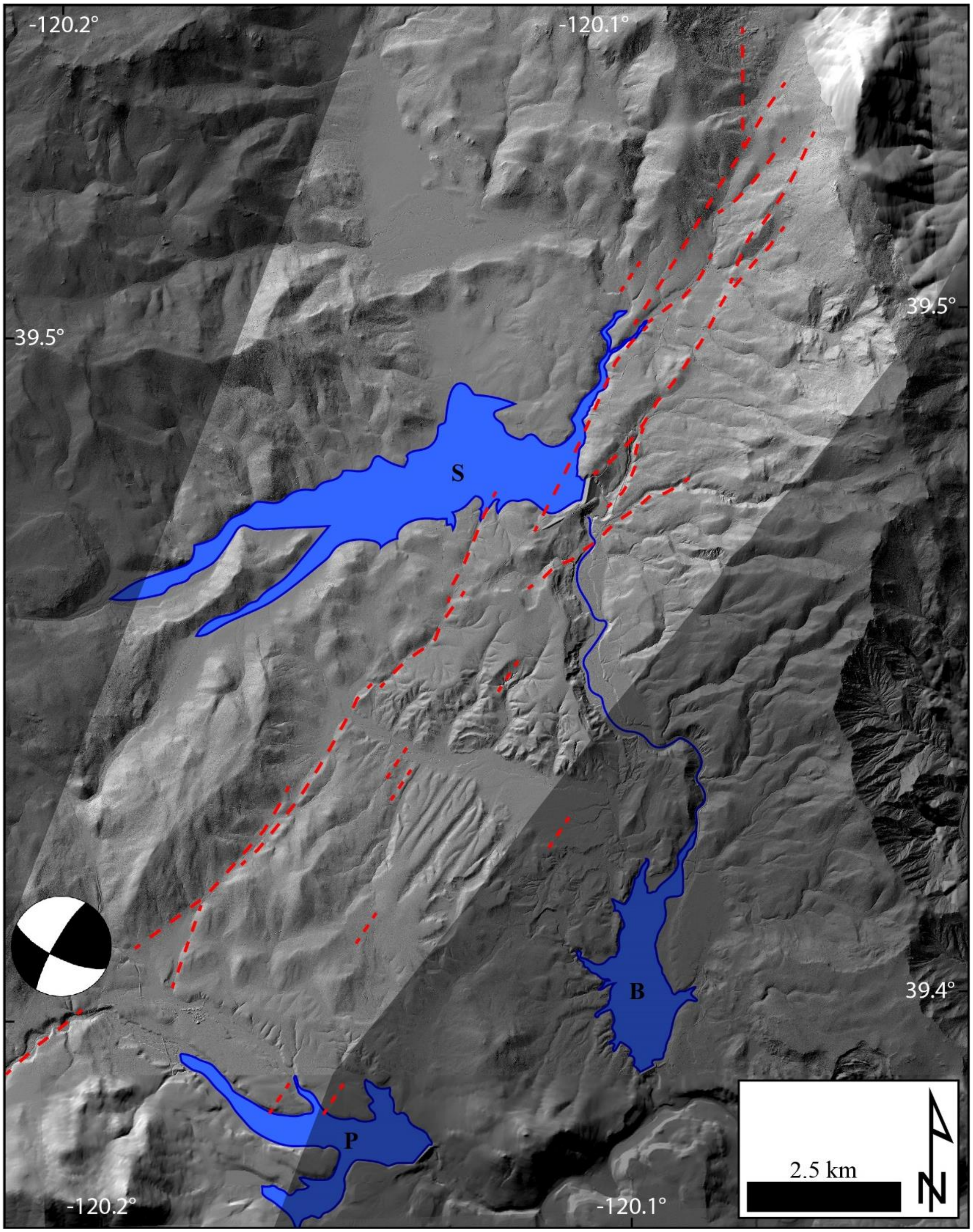

Figure 9. Hillshade image of the seismo-lineament for S3. This M4.0 earthquake occurred on 7/3/1983 at a depth of 8.73 km. The dashed red curves are geomorphic lineaments inferred to be related to the DVF (Hawkins, 1986, p. 66).

Event S5, like S2, has a fault-plane solution with only a moderate dip angle and relatively large orientation uncertainties. The S5 seismo-lineament is broad, has a significant overlap with the S1 seismo-lineament, but offers little additional resolution regarding the location of the DVF (Figure 10). The fault plane solution indicates oblique displacement with reverse dip-slip and sinistral strike-slip components.

There are three posted focal mechanisms for the M3.1 earthquake of August 6, 1993 — S6, S7, and S8 (Table 2). The rake angles for S6 and S7 indicate a dominant dip-slip component, and the fault-plane solutions are moderately dipping surfaces. Hence, S6 and S7 were interpreted to be inconsistent with the fault plane solution for the Truckee earthquake. The seismo-lineament for event S8 is relatively narrow yet overlaps substantially with S1 (Figure 11). Event S8 involved sinistral shear on a vertical or near-vertical plane.

There are two posted focal mechanism solutions for the M3.7 earthquake of June 12, 2004, which has a reported depth of ~7.3 km — S11 and S12 (Table 2). The S12 solution is for a reverse oblique fault with a dip angle of 63°±10°, and is not considered likely for an earthquake on the DVF. The S11 solution has large uncertainties in its fault plane solution, which indicates sinistral shear with a minor component of normal motion on a steeply dipping fault surface. The broad seismo-lineament of S11 overlaps that of the S1 event, and the S11 epicenter is in the area of the suspected DVF trace (Figure 12).

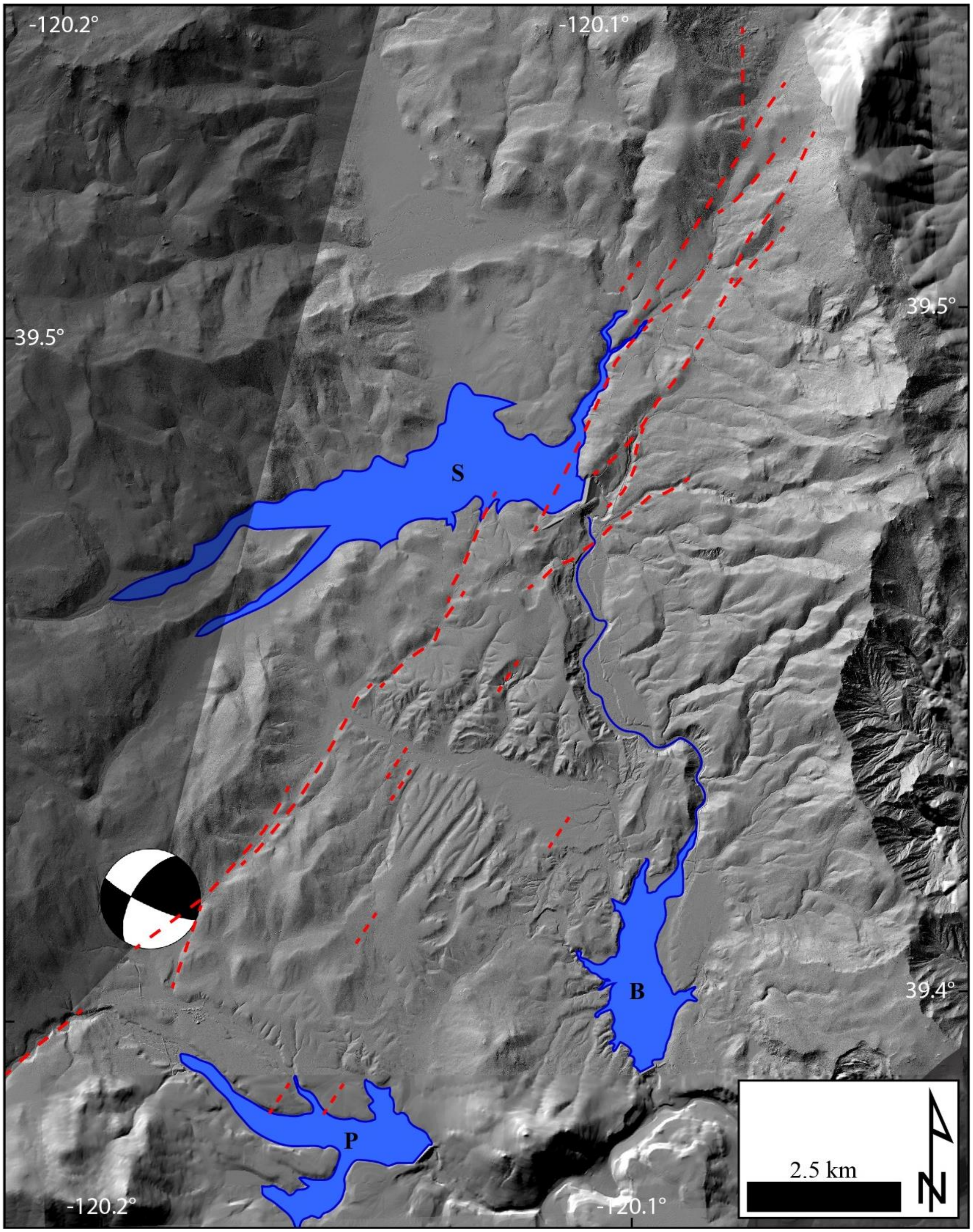

Figure 10. Hillshade image of the seismo-lineament for S5. This M3.2 earthquake occurred on 8/30/1992 at a depth of 5.344 km. The dashed red curves are geomorphic lineaments inferred to be related to the DVF (Hawkins, 1986, p. 66).

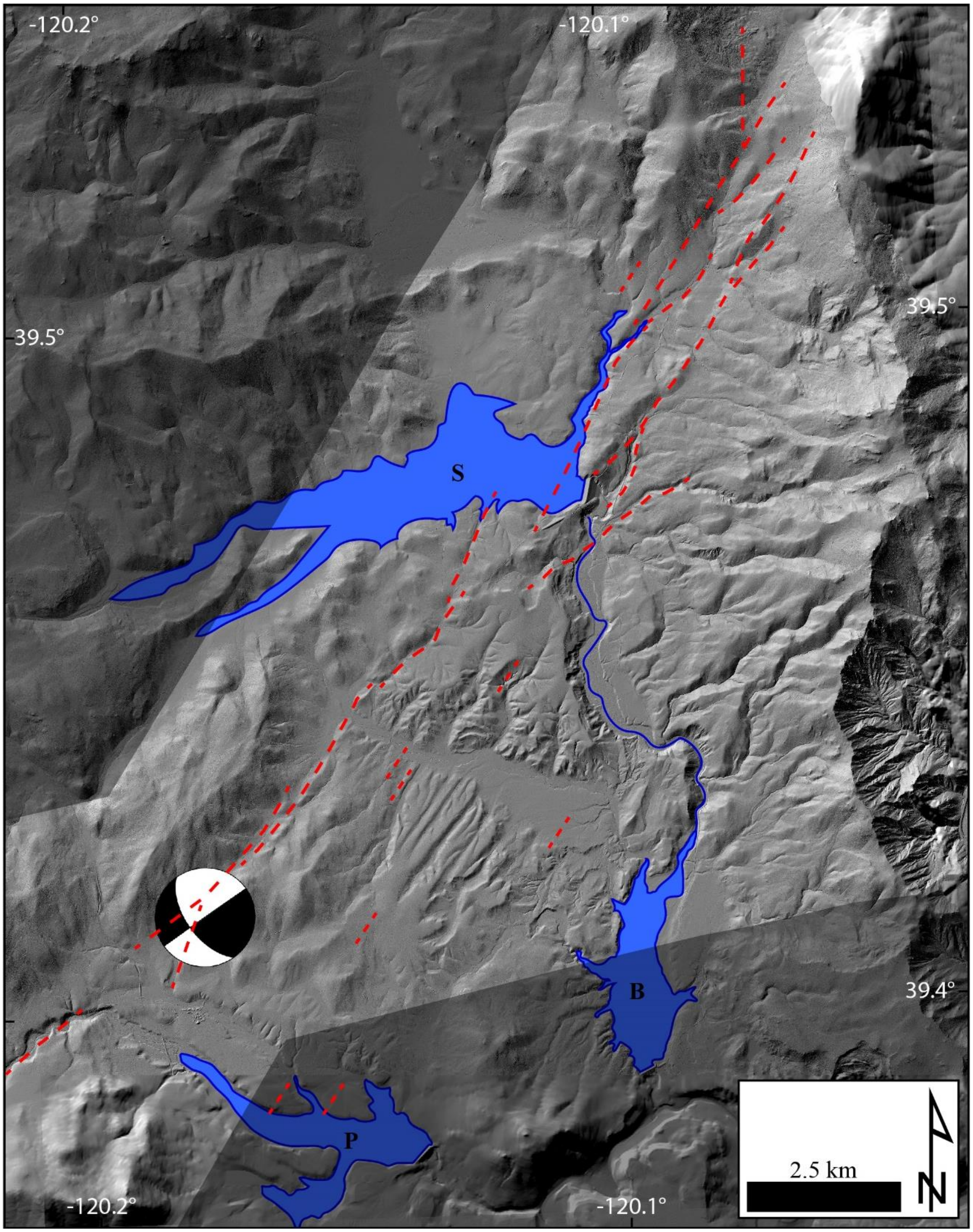

Figure 11. Hillshade image of the seismo-lineament for S8. This M3.1 earthquake occurred on 8/6/1993 at a depth of 0.368 km. The dashed red curves are geomorphic lineaments inferred to be related to the DVF (Hawkins, 1986, p. 66).

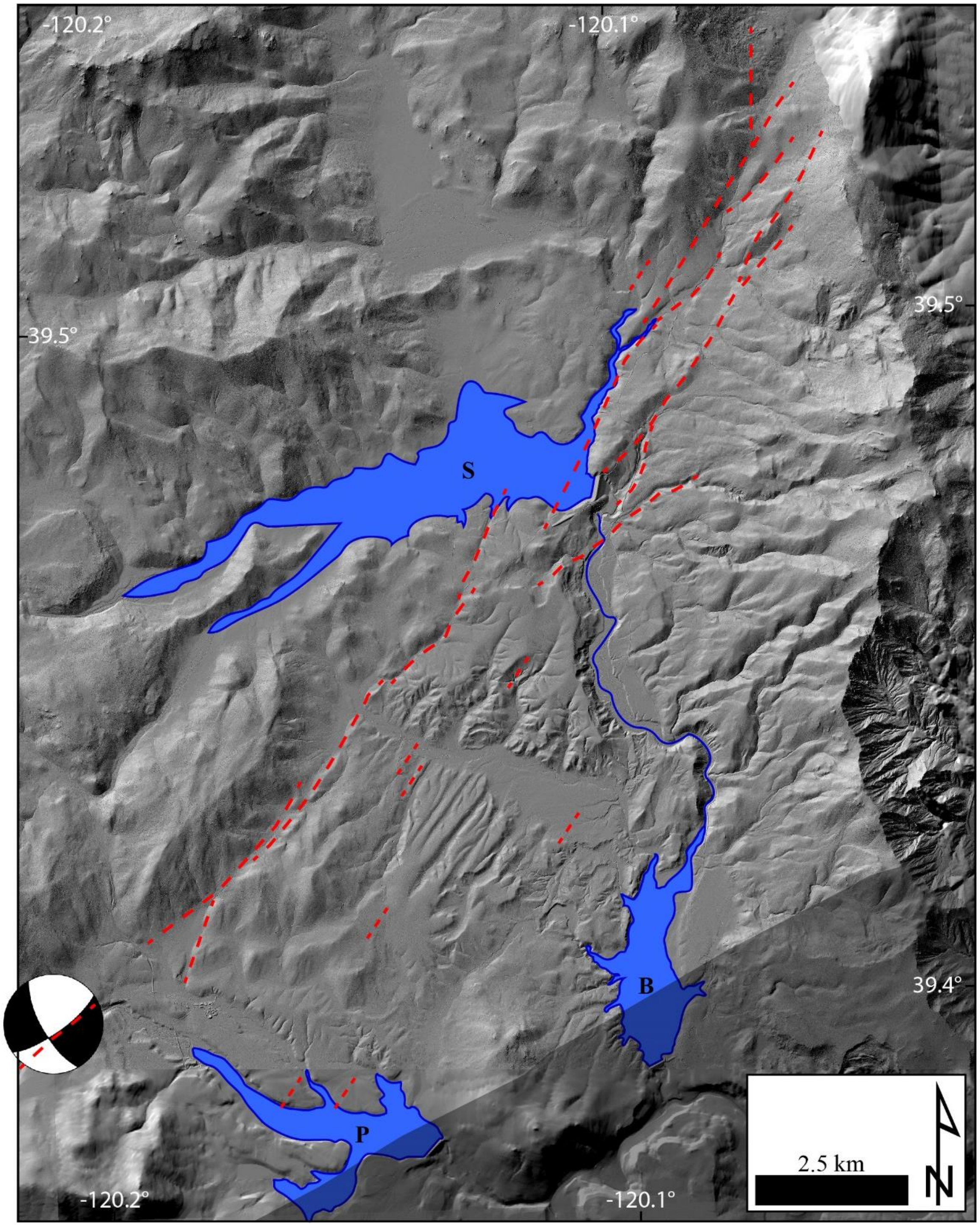

Figure 12. Hillshade image of the seismo-lineament for S11. This M3.7 earthquake occurred on 6/12/2004 at a depth of 7.292 km. The dashed red curves are geomorphic lineaments inferred to be related to the DVF (Hawkins, 1986, p. 66).

The focal location of event S13 is well constrained (Table 1) and is more than 1 km east or southeast of other earthquakes that are interpreted to have occurred along the DVF, although the unstated (but probably substantial) uncertainty in the focal location of S1 requires that caution be exercised. The orientation uncertainties in the fault plane solution for S13 are relatively large, so the seismo-lineament is quite broad and includes that of S1 (Figure 13). Event S13 involved sinistral shear on a fault plane that was probably steeply inclined.

The seismo-lineament associated with S14 displays only minor overlap with that of S1 (Figure 14). This seismo-lineament is not well spatially correlated to the DVF, but might be associated with a closely parallel fault to the southeast of the DVF. A fault with a RHR strike of 23°±13° and dip angle of 86°±13° was observed in an outcrop located above the south side of the Little Truckee River at approximately 39.439°N, 120.097°W, within the S13 and S14 seismo-lineaments. The orientation of that fault surface is not parallel with the fault-plane solution to event S14, which indicated sinistral shear on a steeply dipping plane. The measured orientation of the fault is more consistent with the orientation of the S13 fault plane solution.

The seismo-lineaments associated with S1, S2, S3, S5, S8, and S11 overlap so that a composite map provides a useful idea of where to look for the trace of a fault that might have generated all of these earthquakes (Figure 15). These epicenters are all located along a generally linear trend that is similar to the mean strike of the S1 fault plane solution. The composite seismo-lineament for these events offers a useful constraint in the search for the ground surface trace of the DVF.

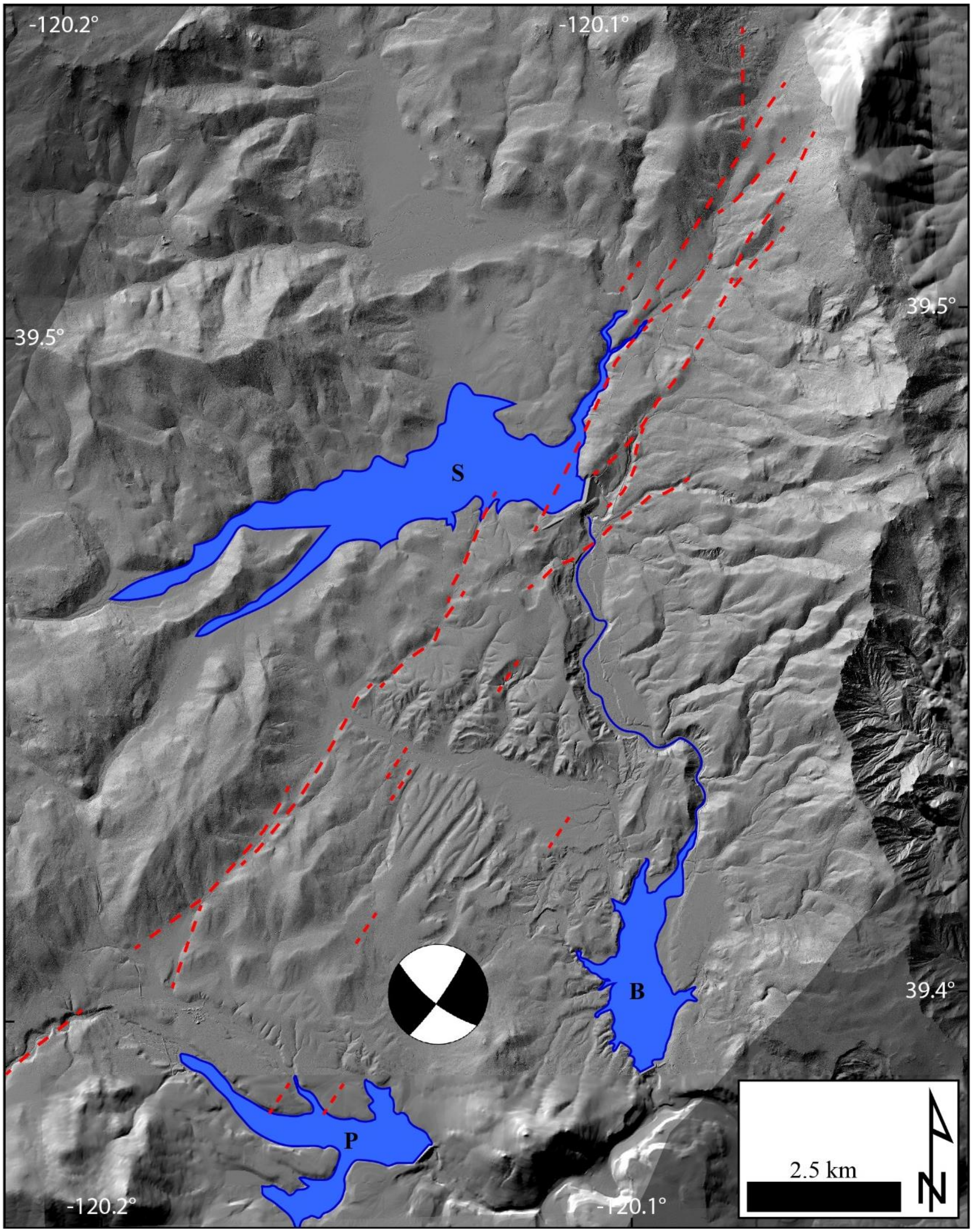

Figure 13. Hillshade image of the seismo-lineament for S13. This M2.7 earthquake occurred on 11/22/2011 at a depth of 10.139 km. The dashed red curves are geomorphic lineaments inferred to be related to the DVF (Hawkins, 1986, p. 66).

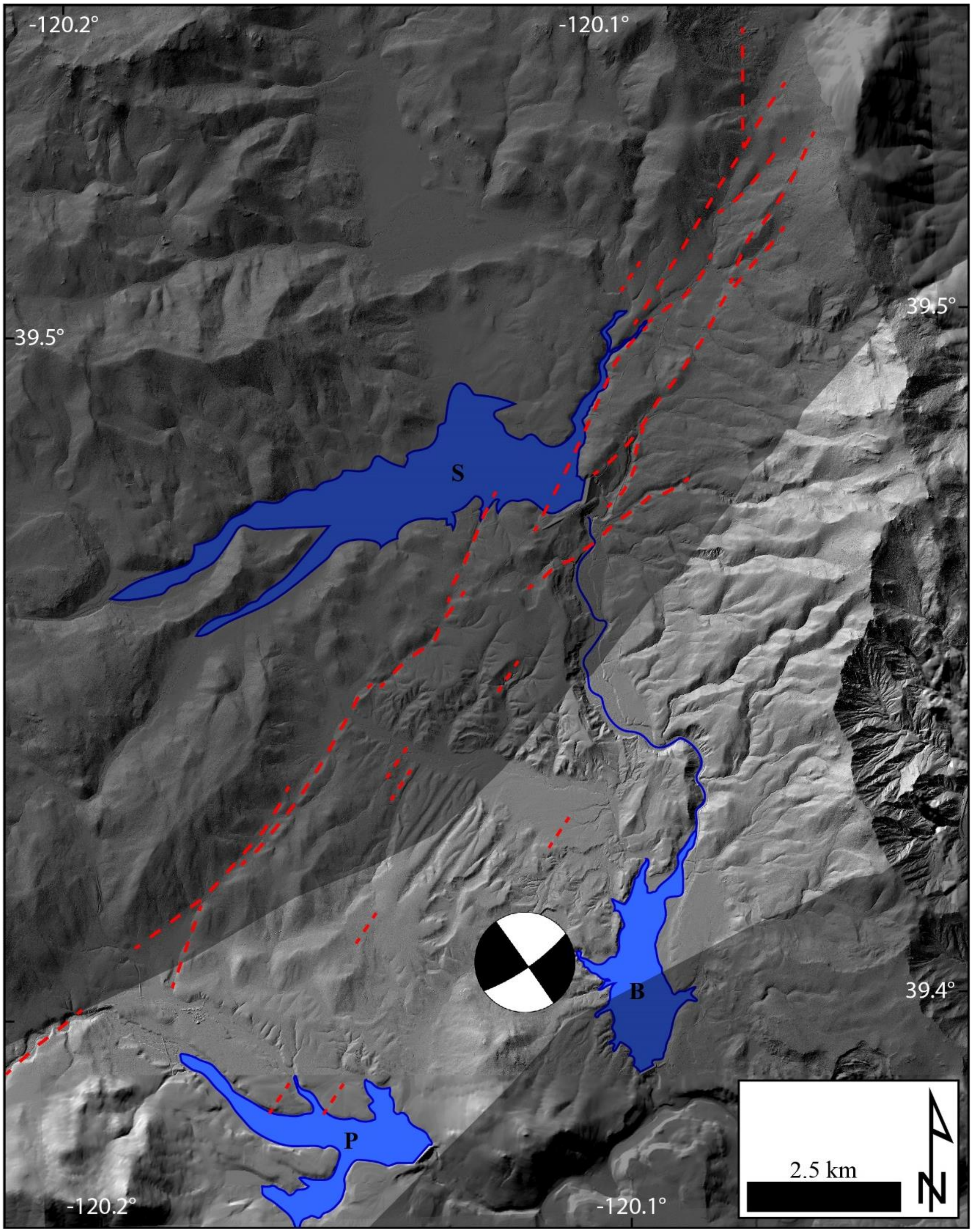

Figure 14. Hillshade image of the seismo-lineament for S14. This M3.0 earthquake occurred on 12/23/2011 at a depth of .882 km. The dashed red curves are geomorphic lineaments inferred to be related to the DVF (Hawkins, 1986, p. 66).

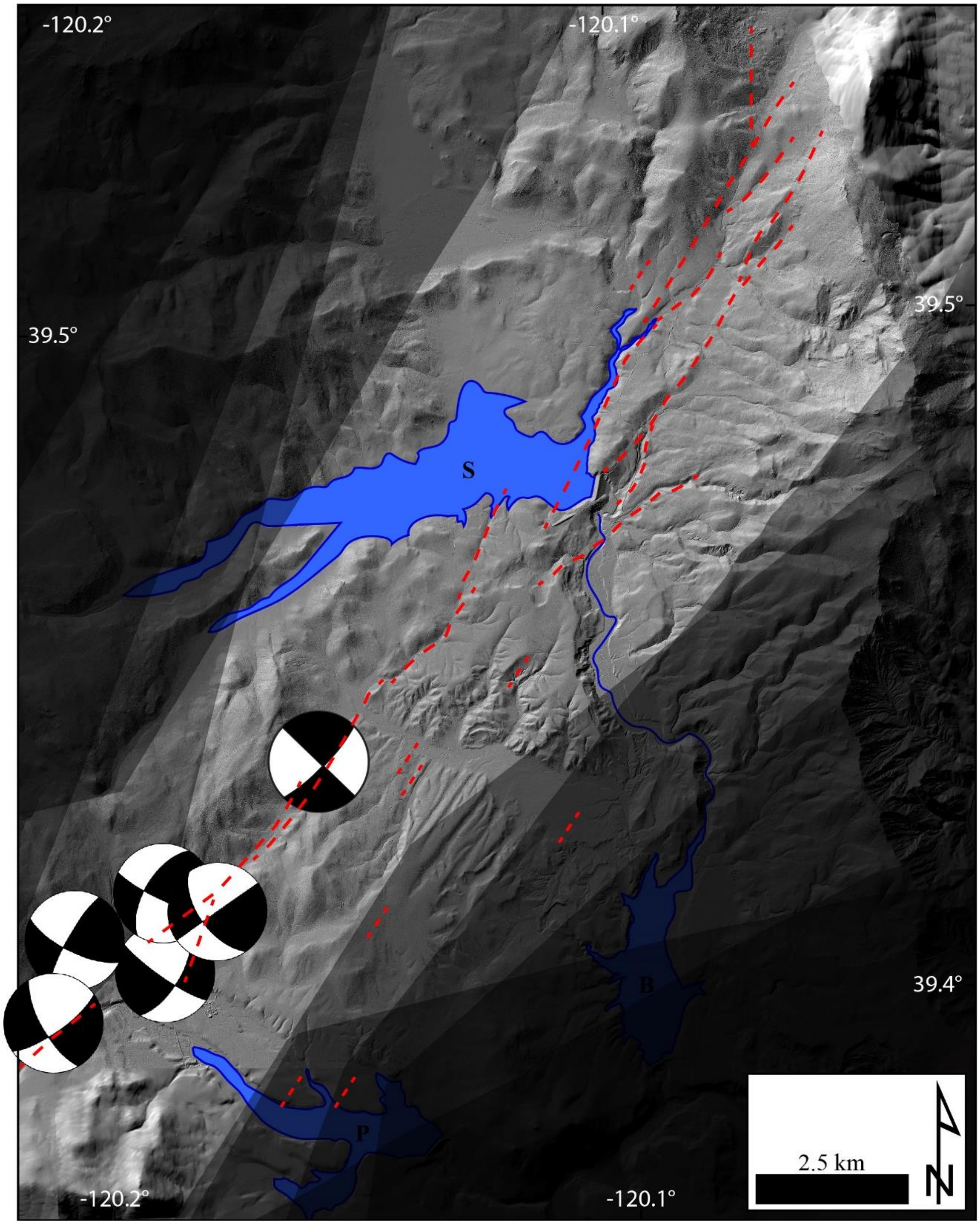

Figure 15. Hillshade image of the seismo-lineaments for S1, S2, S3, S5, S8, and S11. The dashed red curves are geomorphic lineaments inferred to be related to the DVF (Hawkins, 1986, p. 66).

Structural-Geomorphic Analysis

Various geomorphic indictors of faulting are described in the following paragraphs. These topographic features might indicate left lateral shear consistent with the understood motion of the Dog Valley Fault (DVF). There are a total of 28 features described in this thesis that are shown in detail in six figures. Figure 16 shows the relative locations for the subsequent six figures. The features are described in spatial order from the southwest to the northeast. Numerical descriptions are measured in ArcMAP 10.4.1 using the Identify, COGO Report and Measure tools.

Feature 1 on Figure 17 is a stream draining into the northwestern most arm of Prosser Creek Reservoir. The stream trends 49° for 500 meters from 39.3961°, -120.1685° to 39.3994°, -120.1649°. This stream nearly connects with another stream (feature 2) at higher elevation. This second stream trends 44° for 590 meters from 39.3998°, -120.1645° to 39.4036°, -120.1605°. Directly northeast of feature 2 lies a lower order stream cutting through a higher order stream. This lower order stream (feature 3) trends 35° for 100 meters from 39.4038°, -120.1605° to 39.4046°, -120.1599°. Continuing along this trend lies a step (feature 4) in the hill trending 35° for 65 meters with its midpoint located at 39.4055°, -120.1589°. This step is in line with another step (feature 5) trending 45° for 50 meters with its midpoint located at 39.4069°, -120.1575°. A draw (feature 6) between two peaks in the ridge northeast of these steps is located at 39.4098°, -120.1560°.

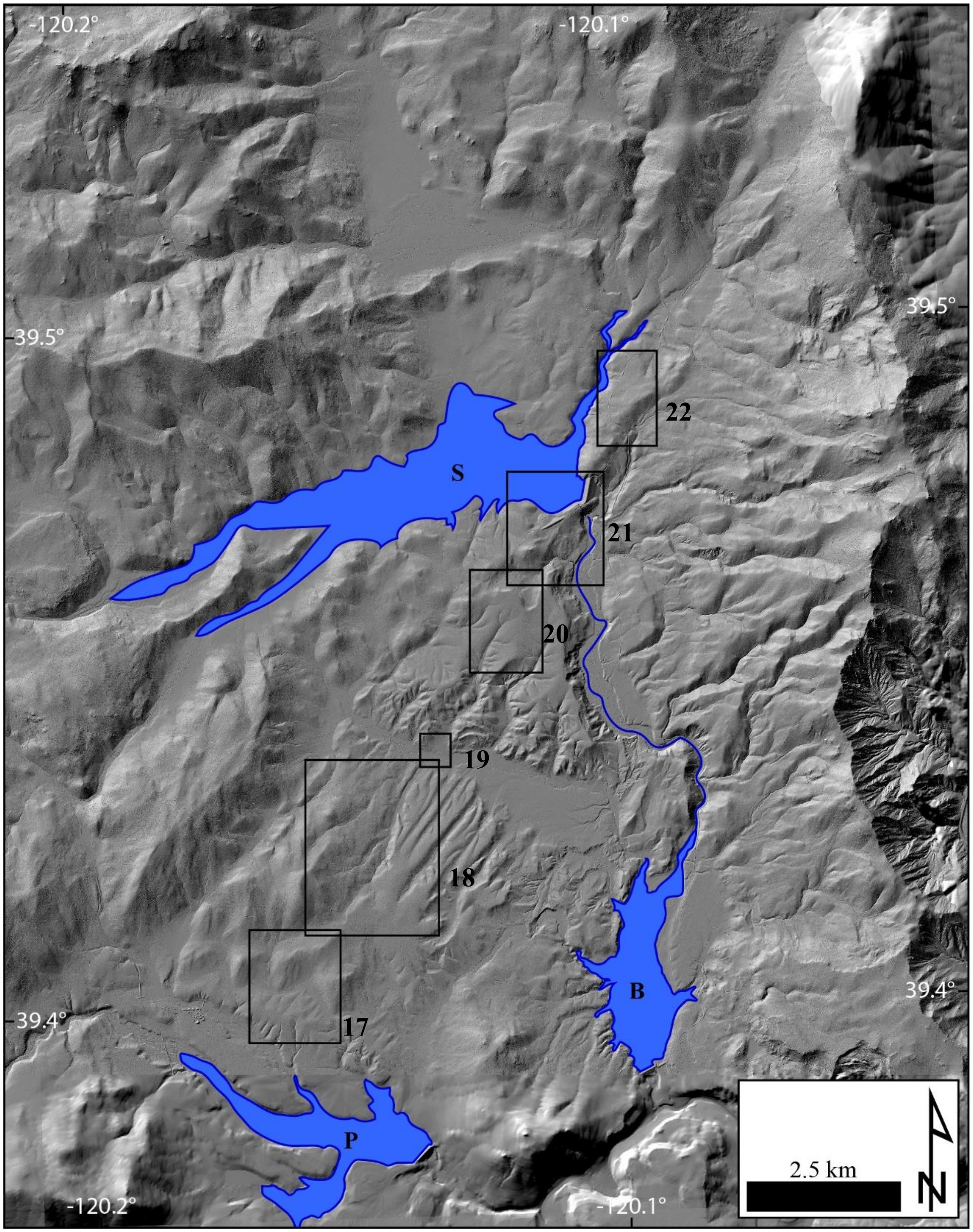

Figure 16. Index map for Figures 17-22.

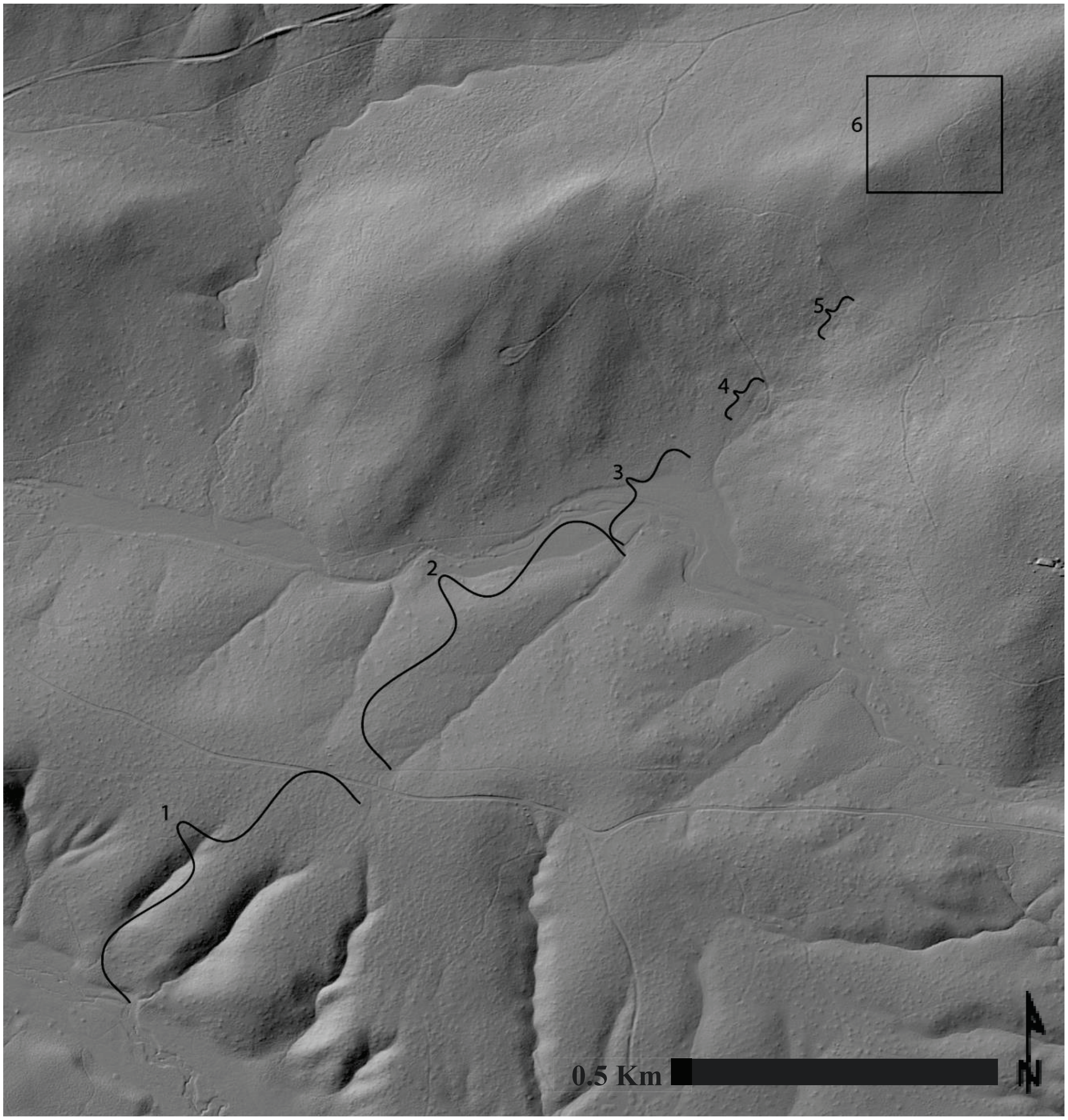

Figure 17. Geomorphic indicators of faulting (1-6). Features 1, 2, and 3 are streams. Feature 3 cross cuts a higher order stream. Features 4 and 5 are steps in the slope. Feature 6 is a draw.

Figure 18 shows a long stream channel (feature 7) at an oblique angle to the dominant drainage pattern. This steam trends 41°±10° for 2 kilometers from 39.4199°, -120.1465° to 39.4355°, -120.1362°. At the mouth of this stream in Figure 19 there is a sharp turn (feature 8) in the major drainage pattern roughly 60° producing a small stream channel that cuts through and connects several channels. This channel trends 35°±3° for 85 meters with its midpoint located at 39.4363°, -120.1352°. Feature 9 is a small straight stream running 30°±5° for 90 meters with its midpoint at 39.4388°, -120.1333° and is aligned with feature 8. Northeast of this point there is a linear vegetation pattern that coincides with a step down to the east (feature 10). This step trends 44°±5° for 65 meters with its midpoint located at 39.4388°, -120.1333°. Feature 11 is a sharp step down to the east that functions as the edge of the flood plain for the stream running through this valley. This step trends 36°±8° for 240 meters with its midpoint located at 39.4406°, -120.1318°.

Figure 20 shows several portions of a stream that align at roughly 45°. Feature 12 is an abrupt step down that acts here as the floodplain wall for the mountain stream. This step trends 44°±5° for 370 meters from 39.4530°, -120.1236° to 39.4556°, -120.1211°. Feature 13 is a step down to the east not coincident with the floodplain. This step trends 38°±3° for 60 meters with its midpoint located at 39.4559°, -120.1207°. A straight section of stream (feature 14) lies 150 meters northeast of feature 13. This stream trends 31°±4° for 105 meters with its midpoint located at 39.4576°, -120.1190°. Feature 15 is a straight section of stream trending 34°±3° for 120 meters with its midpoint located at 39.4616°, -120.1157°. Feature 16 is a step down to the west trending 42°±2° for 83 meters with its midpoint located at 39.4624°, -120.1146°.

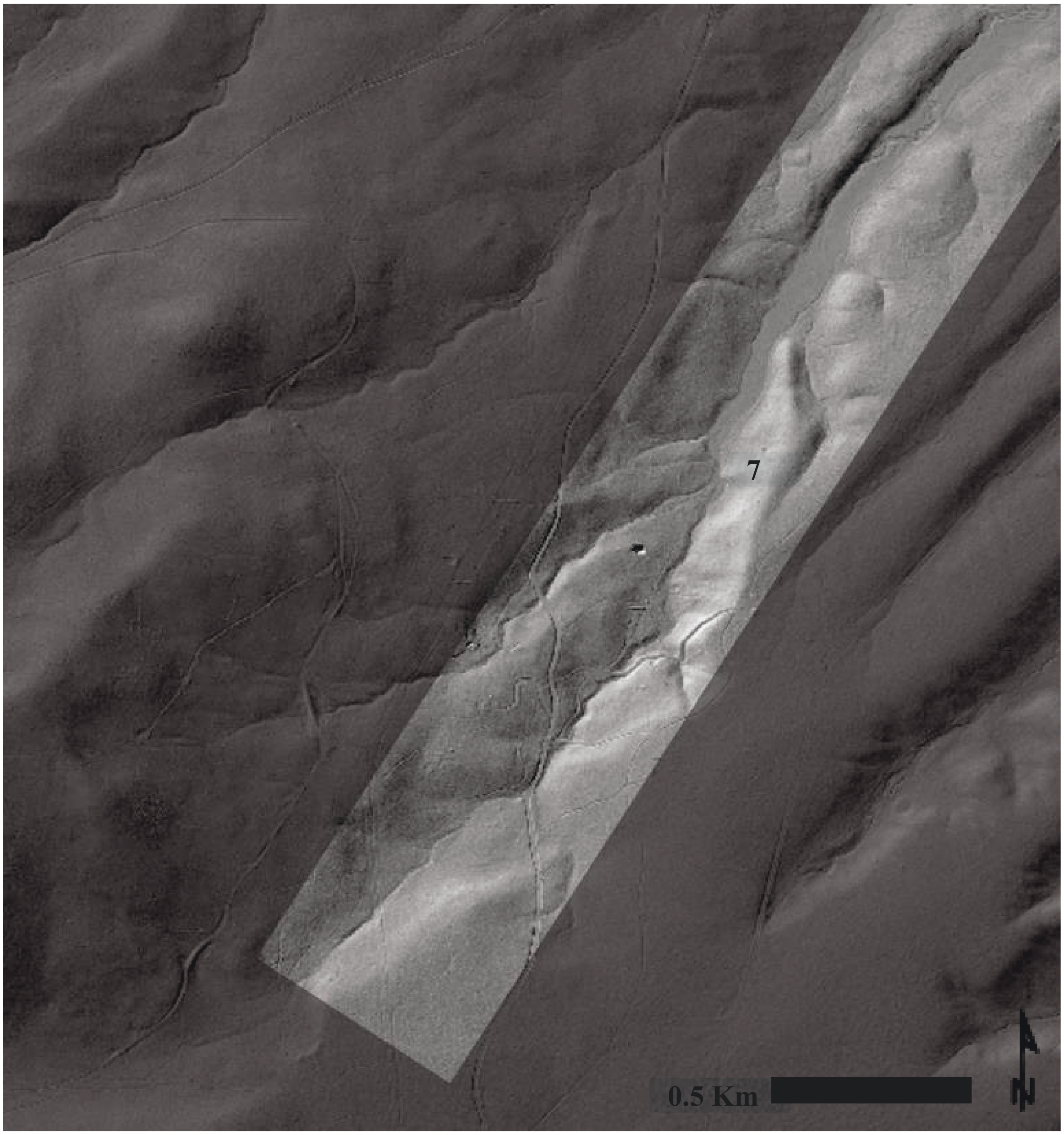

Figure 18. Geomorphic indicators of faulting (7). Long linear valley in line with other geomorphic indicators of faulting.

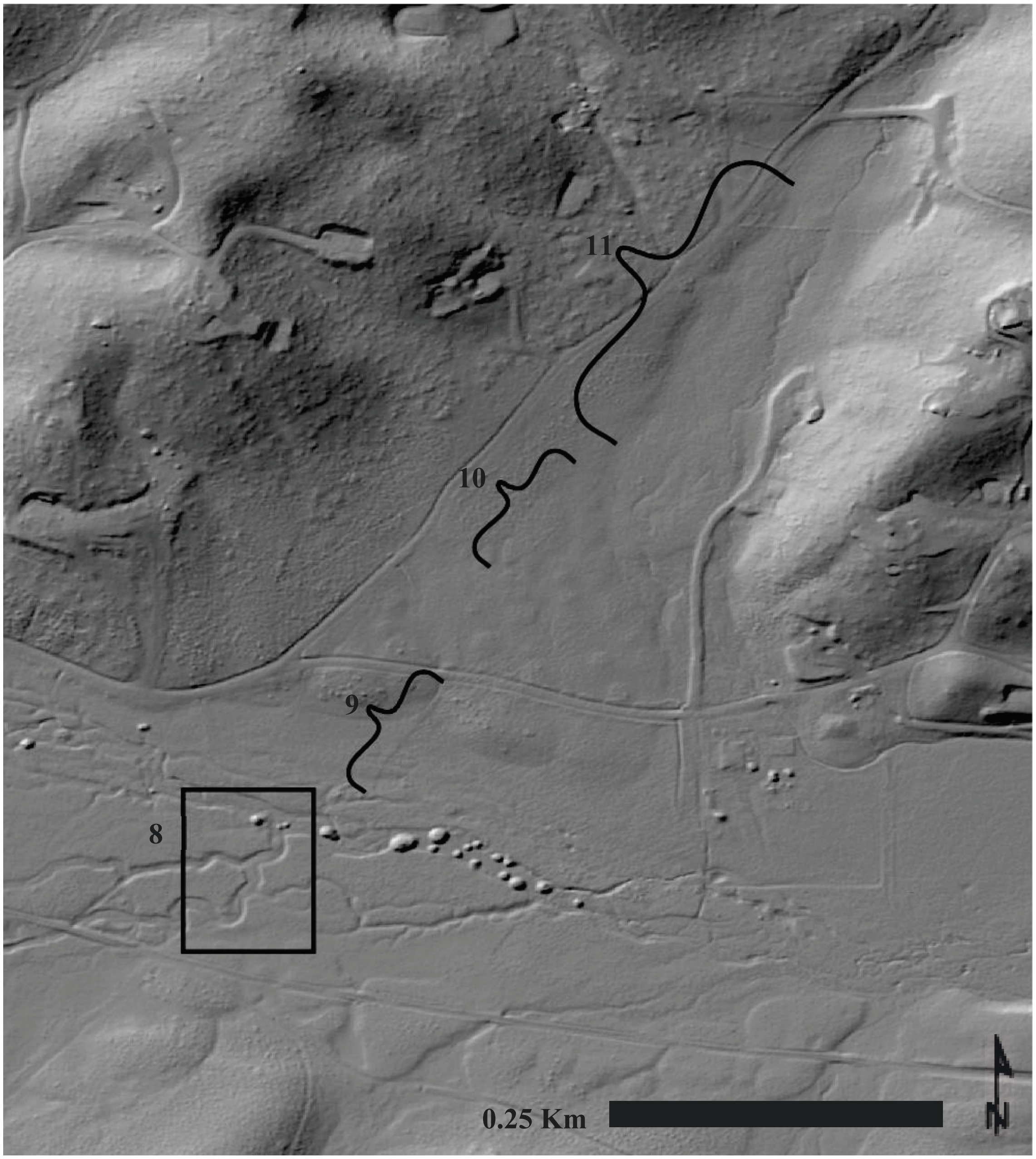

Figure 19. Geomorphic indicators of faulting (8-11). Features 8 and 9 are streams running perpendicular to the major drainage pattern and cross cutting higher order streams. Features 10 and 11 are walls of a floodplain.

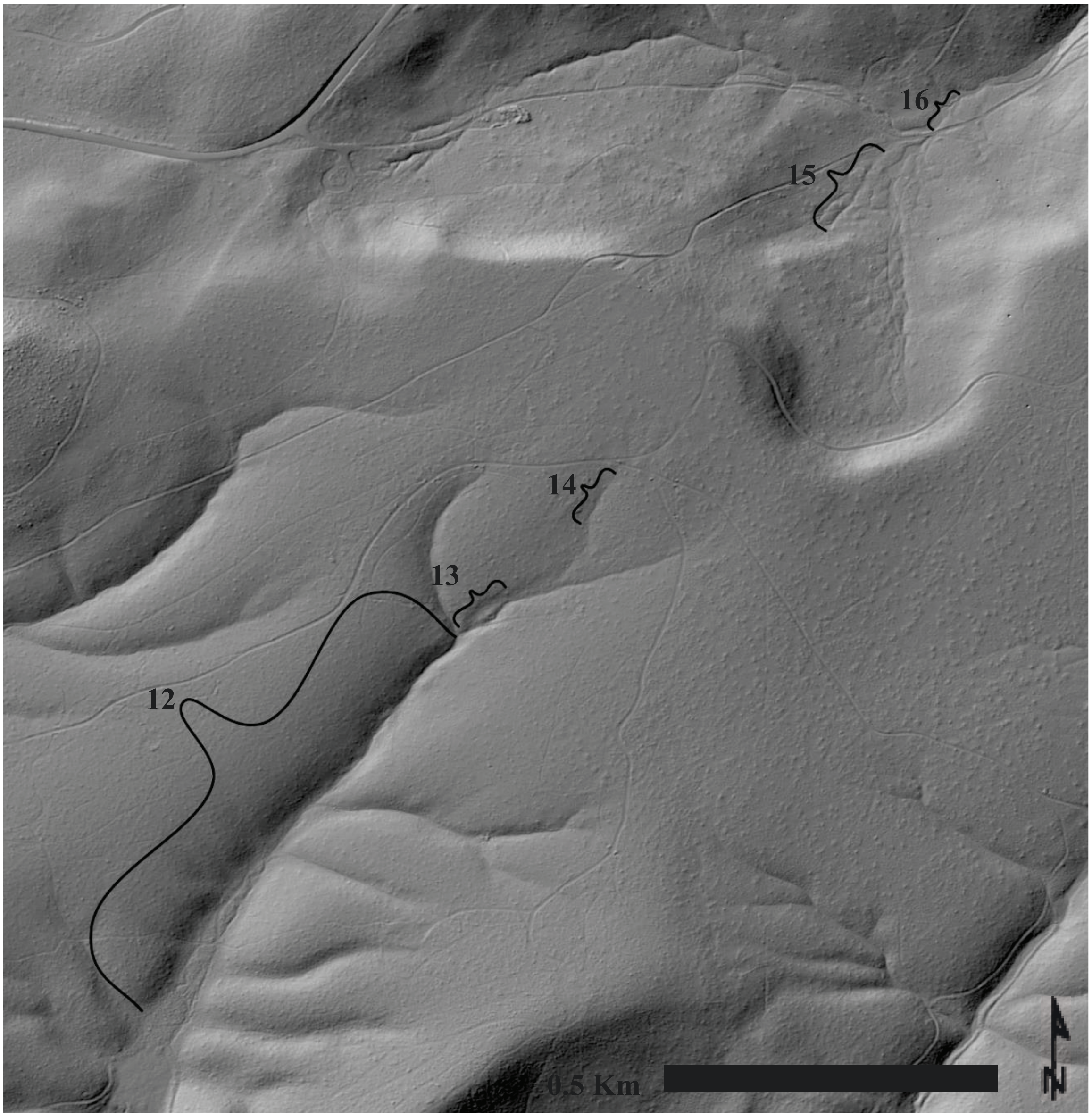

Figure 20. Geomorphic indicators of faulting (12-16). Feature 12 is a floodplain wall. Features 14-16 are straight sections of sttreams. Feature 13 is a step that might have previously been the floodplain of the nearby stream.

Feature 17 in Figure 21 is a ridge trending 33°±5° for 820 meters from 39.4633°, -120.1136° to 39.4699°, -120.1093°. Feature 18 is the abrupt transition from slope to flat with a linear arrangement of trees on the southwest tip creating a line that trends 28°±4° for 85 meters with its midpoint located at 39.4686°, -120.1096°. Feature 19 is a line of trees in a slight linear depression on the high point of a hill. This feature trends 33°±4° for 220 meters with its midpoint located at 39.4705°, -120.1082°. Feature 20 is a step down to the east coincident with a linear arrangement of trees trending 28°±8° for 90 meters with its midpoint located at 39.4722°, -120.1071°. In the feature 21 box there are several linear steps down to the west trending 30°±10° 20 to 30 meters long. This box encompasses F8SD, F7PF, and F6SH, which have trends of 13°±6°, 16°±12°, and ~30°, respectively. The midpoint of this box is 39.4732°, -120.1064°. F4ND is feature 22. There is a linear step down to the east that aligns with this fault and extends into the top of the hill. A linear depression parallels the step 15 meters to the east. The depression is feature 23. The step trends 23°±5° for 70 meters and the draw trends 25°±5° for 70 meters. F4ND trends 4°±4°. The midpoint for the step is 39.4771°, -120.1041° and the midpoint for the draw is 39.4772°, -120.1038°.

Figure 22 shows F1RE and F2RW in the roadcut at feature 24. This feature includes a linear pattern of vegetation in line with the faults. These faults have a mean orientation of 9°±12° and are located at 39.4846°, -120.0978°. Feature 25 is a small stream running perpendicular to higher order streams and the main drainage pattern. This stream trends 43°±10° for 370 meters with its midpoint located at 39.4888°, -120.0942°. Feature 26 is a line of trees and other vegetation that trends 20°±5° for 80 meters with its midpoint located at 39.4912°, -120.0928°. Feature 27 is a linear depression in the hillside that trends 42°±5° for 65 meters with its midpoint located at 39.4919°, -120.0923°. Feature 28 is a linear depression not coincident with the stream trending 24°±5° for 95 meters with its midpoint located at 39.4928°, -120.0918°.

The overall trend of these geomorphic indicators of faulting is 38°±3° over a lateral distance of 12.5 kilometers. This trend is plotted in Figure 23. The red curve connects each of the 28 structural-geomorphic indicators of faulting.

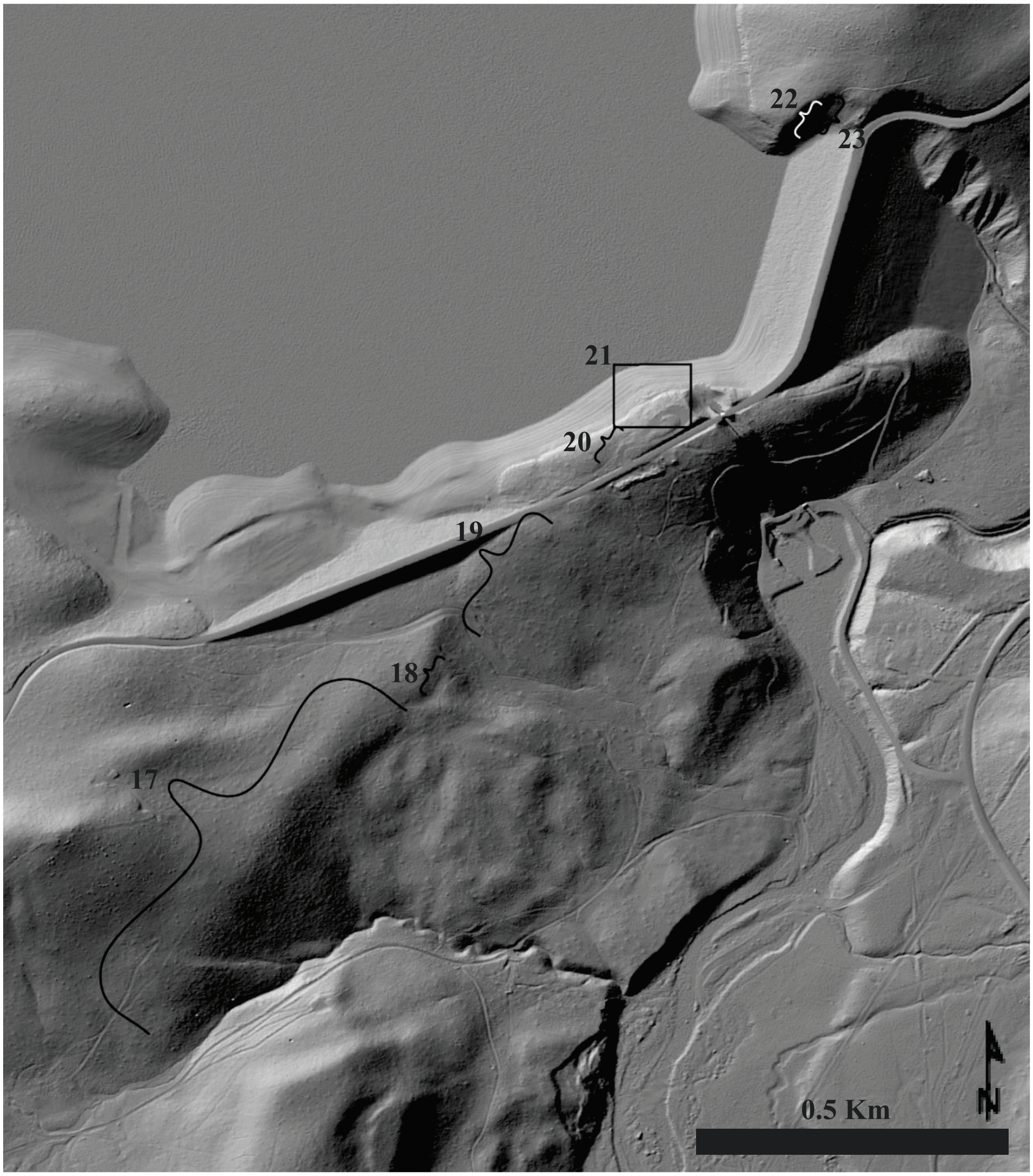

Figure 21. Geomorphic indicators of faulting (17-23). Feature 17 is a ridge. Feature 18 is a linear vegetation trend in line with a dramatic step down to the east. Feature 19 is a linear vegetation trend. Feature 20 is a linear vegetation trend in line with a step down to the east. Feature 21 is a group of faults found on the south abutment of the main dam (F8SD, F7PF, F6SF, F5SP). Feature 22 is F4ND and its visible step down to the east. Feature 23 is a draw directly east of the fault.

Figure 22. Geomorphic indicators of faulting (24-28). Feature 22 is faults F1RE, F2RW, and F3RW in line with a linear vegetation trend. Feature 23 is a stream running perpendicular to the drainage patern. Feature 24 is a straight section of stream. Feature 25 is a linear depression.

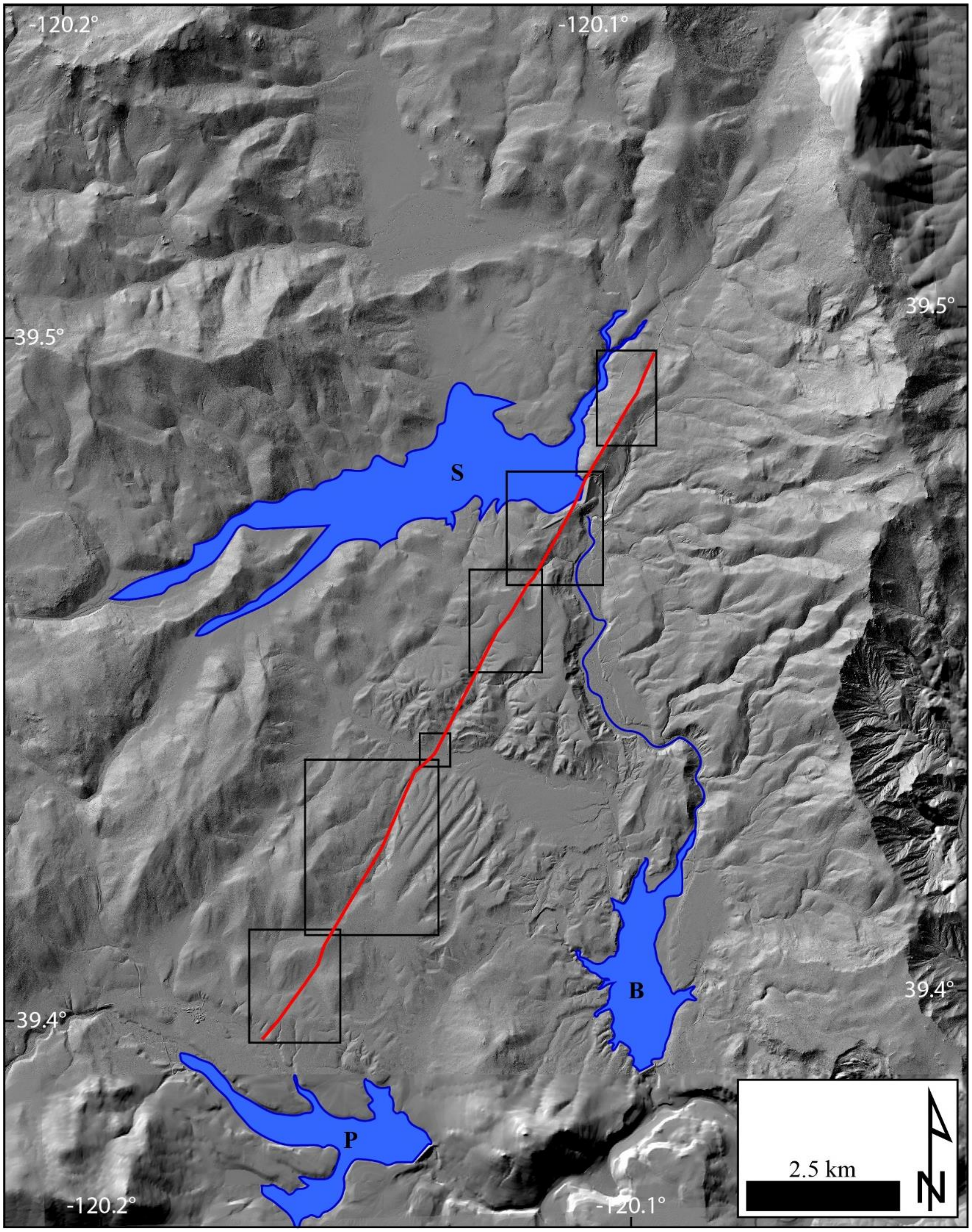

Figure 23. Linear trend of 28 geomorphic indicators of faulting. The red line runs through the 28 geomorphic indicators of faulting found in the structural-geomorphic analysis and in field work as described in this section.

Field Observations

The naming convention for faults found during this field work and used in the study is as follows. Three letters and a number are assigned to each fault; fault "F4ND" will be used as an example. The first letter "F" stands for fault, and is used to distinguish these features from other numbered items in this thesis. Numbers run from north to south, meaning the northern most fault found in this field work is #1. F4ND is thus the fourth fault from the north used in this study. The last two letters are initials pertinent to the location of the fault. "ND" here stands for <u>n</u>orth abutment of the <u>d</u>am. F4ND is the fourth northernmost fault in the study area located at the north abutment of the Stampede Dam. A complete list of the faults found and used in this study is presented in Table 5. Spatial relationships are shown in Figure 24.

Table 5. Data for faults found in the field work portion of this study.

ID	Strike/Dip	Rake	Location (UTM)	Latitude, Longitude
F1RE	192°±15°/85°±15°	N/A	10S 749588 4373581	39.475641, -120.0983585
F2RW	9° ±12°/82°E ±12°	-6°±6°	10S 749602 4374546	39.484321, 120.09783475
F3RW	306°±11°/88°±4°	N/A	10S 749602 4374546	39.484321, 120.09783475
F4ND	184°±4°/89°±4°	-7°±13°	10S 749096 4373715	39.476980, -120.1039986
F5SF	~30°/90°	N/A	10S 748900 4373269	39.473032, -120.1064638
F6SP	~330°/90°	N/A	10S 748946 4373278	39.473100, -120.1059263
F7PF	16°±12°/78°±12°	2°±6°	10S 748900 4373269	39.473032, -120.1064638
F8SD	13° ±6°/87°E ±6°	2°±8°	10S 748901 4373253	39.472888, -120.1064582
F9LT	23° ±13°/86°E ±13°	N/A	10S 749815 4369499	39.438841, -120.0972500

Fault data was analyzed using a statistical method developed by Fisher (1953) as described by Cronin (2008). UTM location data was measured on site and later converted to Latitude and Longitude using a UTM to Lat/Lon Calculator (Dutch 2015).

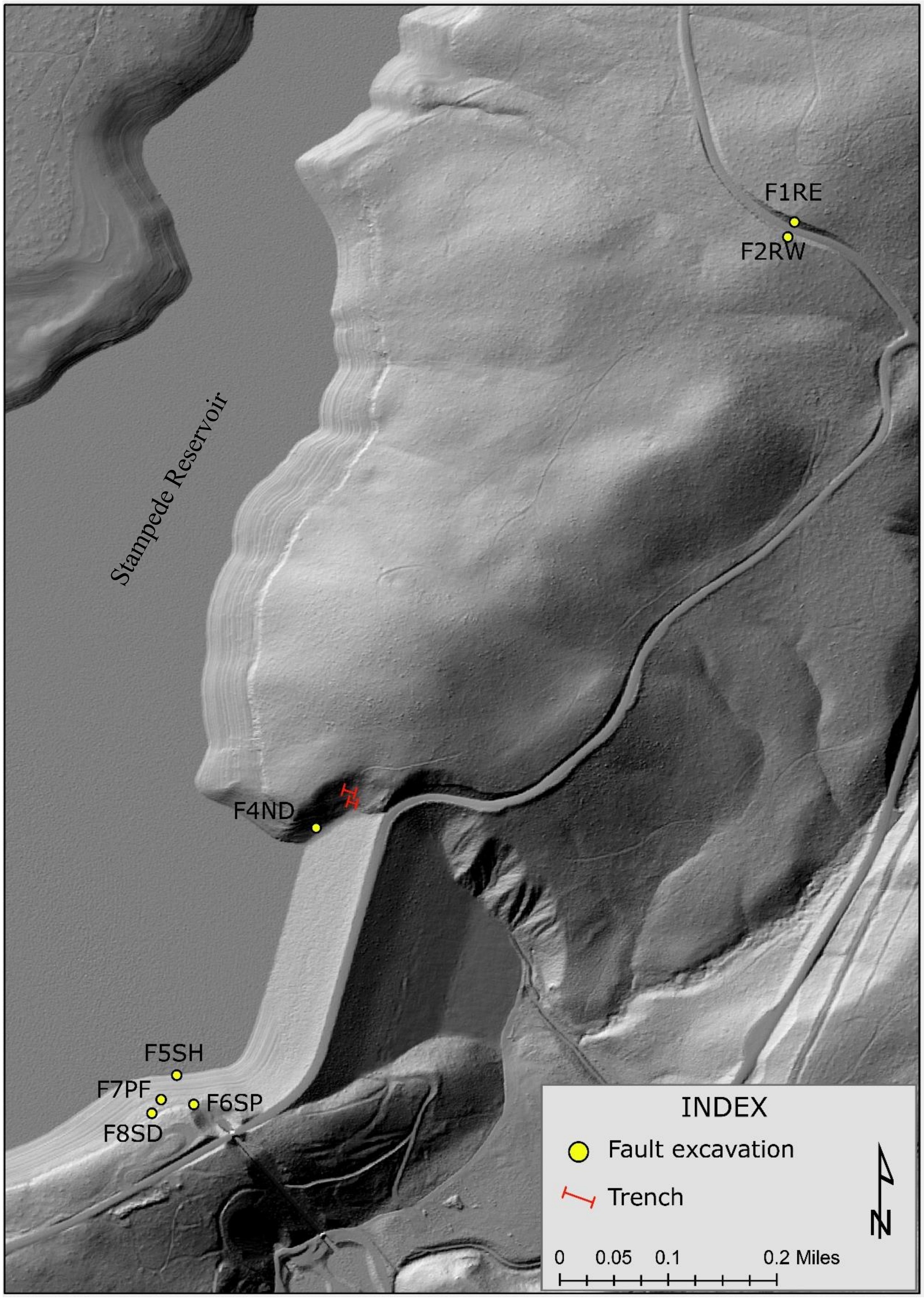

Figure 24. Spatial relationship of faults found in the field work portion of this research. Eight fault excavation sites are shown as yellow circles. Trenches are displayed by red lines. The basemap is an improved hillshade image illuminated at 315° with a sun angle of 30° above the horizon.

Geological reconnaissance field mapping exercises occurred in Hoke Valley along the eastern shoreline of the Stampede Reservoir and the northwest shoreline of Prosser Creek Reservoir. A map showing the area inspected is shown in Figure 25A. The Stampede Reservoir inspection began at the high water mark in Hoke Valley at Stampede Dam Road. This inspection included a search for lineaments in the recently exposed shoreface, all outcrop, and in stream channels cutting through unconsolidated cross stratified sand and gravel. Two faults were found in this inspection. One has a strike and dip of 313°, 38° located at UTM 10S 749407 4376052 and the other has a strike and dip of 351°, 72° located at UTM 10S 749213 4374856. Fault planes were exposed using metal and plastic putty knives.

The northwest shoreline of Prosser Creek was inspected in the same way as the geological reconnaissance mapping performed at Stampede Reservoir (Figure 25B). No faults were found in this inspection. Several drainages with strikes similar to the DVF come into the reservoir along this shoreline. No faults consistent with the understood mechanics of the DVF were located in these areas.

F4ND was found at 12:00 on September 24, 2016 at UTM 10S 0749096 4373715. The untouched linear feature that distinguished this fault from its surroundings was a change in vegetation density (Figure 26). The change occurs across a lineament trending roughly 10°. Vegetation to the east of the lineament is relatively dense when compared to vegetation to the west. The color of the bare earth also contrasts across this lineament, with a light gray-green ignimbrite to the west and medium-dark brown soil to the east. This lineament was excavated initially with a steel putty knife (Figure 26).

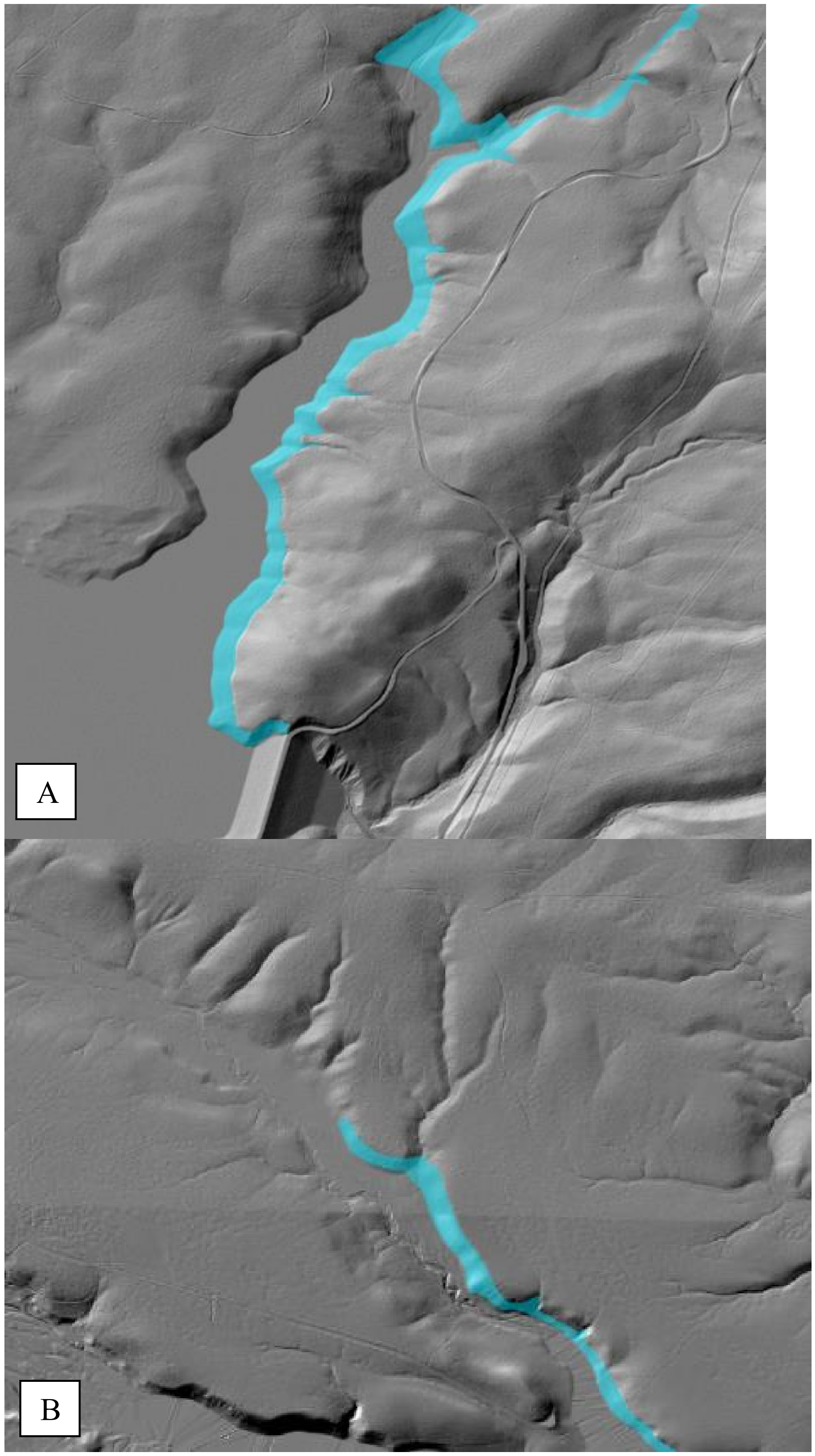

Figure 25. Geological reconnaissance field mapping. A: Stampede Reservoir. The area inspected is highlighted in blue. Recent decreases in lake level (>15 m) allowed for a much greater area to be searched than has previously been available. B: Prosser Creek Reservoir. The area searched in shown in blue and continues to the east off of the map to the middle of the lake. This field inspection did not cover the drainages proposed by Hawkins et al., (1986) to contain the ground surface trace of the DVF.

Figure 26. F4ND undisturbed. This photograph shows the undisturbed F4ND, taken near the shoreline facing roughly 10°. Notice the linear change in vegetation and topography from left to right. The poorly vegetated ignimbrite on the left sits roughly 46 cm higher in elevation than the better vegetated ignimbrite on the right. This ignimbrite on the right has several centimeters of soil ranging from 1 cm to 15 cm deep possibly due to the ability of precipitous runoff to transport sediment onto this block because of its lower

The rock surface on the east was covered with several centimeters of soil and had a total 30 cm ± 10 cm vertical offset from the top of this ignimbrite to the top of the ignimbrite to the west. The fault was excavated in two locations. The southern excavation was 30 cm deep, shallowing south, and 1.2 m long (Figure 27). No shear striations were found in this excavation. The gouge was darker than the surrounding

Figure 27. F4ND south excavation. This area received 0.1 cm of precipitation on 22 September 2016, which darkened the gouge, heightening the contrast between gouge and ignimbrite blocks on either side. This photograph was taken on 24 September 2016. The west block was excavated slightly beyond the gouge zone in places in order to produce a cross section to distinguish darker gouge from lighter fault block. The gouge zone here ranges from .6cm to 9.5 cm thick.

material due to approximately 0.1 cm of rain the previous day (NOAA, 2017). The northern excavation was 46 cm deep, shallowing south, and 1.2 m long (Figure 28). The fault core varied between 9 cm and 10 cm wide (Figure 29). The gouge material is light olive gray 5y 5/2 when dry and grayish brown 5yr 3/2 when wet as measured with a Rock Color Chart from The Geological Society of America with genuine Munsell color chips. Sub-horizontal (-7° ±13°) shear striations were found beginning at 20 cm depth and measured on the east wall of the fault as shown in Figures 30 and 31.

From this fault a line was extended across the lake along strike to estimate the most likely location for a fault on the south side of the dam. The first fault that was located on the south side of the dam was F6SP at UTM 10S 748946 4373278. This is a near vertical fault trending 330°, near perpendicular to the proposed trend of the DVF.

F8SD, was found a few meters southwest of the wooden observation tower on the right abutment of the Stampede Dam at UTM 10S 748901 4373253 (Figure 32, 33). This is a vertical fault striking 13° ±6° and dipping 87°E ±6°, with sub-horizontal shear striations measured at 2°±8° (Figure 34). The topographic feature associated with this fault is a step down from east to west. The west block is roughly 30 cm lower than the east block. The fault was excavated 46 cm deep shallowing north over a lateral distance of 3.7 m. The fault core is consistently 10 cm wide throughout this excavation (Figure 35). Ignimbrites indistinguishable from those at F4ND make up the fault blocks on either side. The gouge material here is moderate yellowish brown 10YR 5/4" when wet and "very pale orange 10YR 8/2" after several days of drying. After eight months drying time the gouge color changed to yellowish gray 5y 8/1.

Figure 28. F4ND north excavation. This photograph shows the upper excavation site of F4ND on the north abutment of the Stampede Dam. The gouge was excavated with the pictured gardener's pick and trowel. The boulder in the center of the photograph has sub-horizontal shear striations. Photograph taken facing east.

Figure 29. F4ND fault core. This photograph displays the width of the fault core after removing the gouge at the upper excavation site of F4ND. The fault core excavation measures 9 cm to 10 cm wide along this portion of F4ND and is 20 cm to 30 cm deep.

Figure 30. F4ND shear striae. This photograph shows the inside of the boulder from Figure 27 with the shear striae traced on a levelled grid. Each striation was measured with a protractor against the grid and results are reported in Table 5.

Figure 31. F4ND shear striae. This fault plane exhibits sub horizontal shear striae as traced on the ignimbrite. These striae were measured off of a leveled horizontal line using a protractor and range from -11° to +2°.

Figure 32. F8SD facing north. This fault was found by extending the fault plane from F4ND across the dam and the lake to this location. The block to the west steps down roughly 61 cm below the eastern block. This photograph was taken several meters southwest of the wooden observation tower on the Stampede Dam facing roughly 10°.

Figure 33. F8SD facing south. This photograph shows the partially excavated F8SD taken facing roughly 190°.

Figure 34. F8SD shear striae. Sub horizontal fault striations are present on this face of the fault ranging from -2° to +5°.

Figure 35. F8SD fault core. The gouge zone in F8SD is consistently 9 cm wide throughout this excavation.

F7PF is at UTM 10S 748900 4373269, between F8SD and the southern shore near the dam (Figure 36). This fault was found by extending the plane of F8SD northward to the shoreline of the lake. There is not one main fault in this location, but rather a compilation of smaller parallel faults with intersecting faults trending 300° (Figure 37). These faults strike 16°±12° and dip 78°±12°. No shear striations were found in this sediment. The sediment was soft and unstable, which resulted in collapsed walls upon each attempt to excavate the fault planes to obtain better data. F5SH is an area where vertical fractures (±20°) cut through ignimbrite in the swash zone trending 30° along this same plane. The bedrock here is highly fractured and did not offer good data. These fractures are located at UTM 10S 748890 4373310.

The plane connecting F7PF, F8SD, and F4ND (Figure 38) is used as evidence to suggest these faults might be portions of one larger and more extensive fault. This plane intersects a road cut on Stampede Dam Rd 1.6 km north of the dam that yielded near vertical faults on either side of the road. F2RW (Figure 39) lies in unconsolidated sand near the soil horizon on the west road cut. Calcareous cement adds fault wall structure. This fault could not be excavated deeper than 20 cm due to the instability of the unconsolidated sediment. F2RW has a strike and dip of 1625°±214° with shear striations measuring -6°±6°. F3RW intersects F2RW at 60° and is equal in magnitude to F2RW (Figure 40).

Figure 36. F7PF to F8SD. This photograph displays the proximity and lateral connectivity of F8SD and F7PF. Faults are traced in black lines. The plane of F8SD is extended by the dashed line.

Figure 37. F7PF facing south. This zone of faulting was found by extending the fault plane from F8SD northward to the shoreline. There is no longer one major fault visible as there is further south at F8SD. Here the shear has been accommodated by multiple near vertical strike slip faults.

Figure 38. F8SD to F4ND. In this photograph the trace of F8SD has been extended northeast near the site of F4ND. The spatial and mechanical relationships between these two faults are used as evidence of their correlation and likelihood of belonging to the same fault system.

Figure 39. F2RW undisturbed. Shown above is the undisturbed F2RW. This fault was found by extending the fault plane at the north abutment of the dam northeast to the road

Figure 40. F2RW excavated. The fault plane would not accept deeper excavations due to its instability and soft sediment structure.

Across the road along strike there is a near vertical fault, F1RE, at UTM 10S 0749588 4374581, which cuts through ignimbrite (Figure 41). The fault core is roughly 10 cm wide and is filled with gouge. A tree above the road cut has propagated its roots through this fault core, damaging the walls of the fault. Further fault wall damage has been caused by an ant hive. The walls of this fault are highly irregular at this location and did not yield good fault measurements. F1RE does show evidence of a vertical fault in ignimbrite with roughly 10 cm of fault gouge consistent with F4ND and F8SD (Figure 42). Between these faults and F4ND there is a draw located at UTM 10S 749255 4374011 between two apparently sinistral offset peaks. No additional evidence of faulting was found along this line.

Another fault, F9LT, was measured at UTM 10S 0749815 4369499. This fault is visible in the cliff across the Little Truckee River from the Stampede Meadows Rd pull off 3.2 km south of the Stampede Dam (Figure 43). A large pine tree grows in this fault with roots running the length of the fault. The northwest fault block has dropped down approximately 0.9 m relative to the southeast block. The soil above the northeast block is loose and broken. This fault has a strike and dip of 23° ±13°/86°E ±13°. No shear striations were found in this fault.

The area directly east of F4ND was trenched to investigate a linear color change in the substrate. This color change is readily visible from the Dam and lies in the draw east of F4ND. Two trenches located at UTM 10S 0749113 4373734 and 10S 0749113 4373727 revealed no faults. These trenches were dug through roughly 1 meter of slump fill with ignimbrite forming the base of each trench for the entire length of the trench. The maximum trench depth was 0.9 m and each trench was 3.7 m long (Figure 24).

Figure 41. F1RE undisturbed. This fault was found by extending the fault plane from the west side of the road across the road to the east. The gouge zone has a tree root growing through it as well as an ant hive.

Figure 42. F1RE excavated. A tree root has preferentially grown through this gouge zone and ants have mined the soft sediment and organic material. These have deformed the walls of the ignimbrite blocks associated with this fault. Because of this deformation the data collected at this site exhibit a high degree of uncertainty.

Figure 43. F9LT facing south. Matthew Strasser is analyzing and measuring the orientation of this fault. Both trees pictured have grown in the fault.

GPS Crustal Strain Analysis

Data accessed on 10 January 2017 from eleven GPS sites were used to perform a crustal strain analysis (UNAVCO, 2017; Nevada Geodetic Laboratory, 2017). The GPS velocities from these stations are measured relative to the North America-fixed reference frame NA12 (Blewitt et al., 2013). The epoch coordinates and velocities from 299 GPS stations are used to define NA12. This reference frame has an increased density from previous reference frames and minimizes apparent rotation of GPS velocities within North America (Blewitt, 2015).

This area exhibits an average horizontal translation velocity of 9.8 mm/yr in the direction of 303.6°. The average velocity of the Pacific Plate at 39.36°N, 120.12°W is 48.3 mm/yr in the direction of 328.1° (DeMets et al, 2010). The average velocity in this study area differs from the average velocity of the Pacific Plate in this region by 38.5 mm/yr and 24.5°. This difference in the velocity fields is consistent with its location within the Northern Walker Lane, an area dominated by right lateral shear. Thirteen of the fourteen GPS station triplets analyzed show clockwise rotation consistent with right lateral deformation.

Table 7 shows the instantaneous horizontal strain rates as derived from MIDAS velocity fields of twelve GPS stations (Blewitt et al, 2016). The maximum horizontal extension lies on the greatest horizontal strain axis $S1_H$. The minimum horizontal extension lies on the least horizontal strain axis and is perpendicular to $S1_H$. Figure 43 demonstrates horizontal strain with a circle drawn inside the triangle formed by a GPS station triplet. As an area undergoes horizontal strain this circle will deform and the resultant shape is an ellipse. The long axis of the ellipse corresponds to $S1_H$, showing the

Table 6. Instantaneous horizontal strain rates derived from PBO and MAGNET velocities.

GPS Station Triplet	Translation Azimuth (°)	Translation Speed (mm/yr)	Rotation Velocity (nano-rad/yr)	Rotation Velocity Uncertainty (nano-rad/yr)	Max Horizontal Extension (n-strain/yr)	Min Horizontal Extension (n-strain/yr)	Area Strain (n-strain/yr)	$S1_H$ Azimuth (°)
GIRL-P149-VRDE	301.9	9.0	-41.22	46.03	8.3857	3.1683	11.5541	111.8
P149-VRDE-SARD	302.6	9.3	-56.57	26.65	15.5191	-28.2813	-12.7621	99.1
P149-SARD-BOOM	304.8	9.5	-22.99	23.73	49.2330	-48.3113	0.9217	80.1
SARD-VRDE-BOCA	302.4	9.5	-39.37	27.18	28.0942	-39.0963	-11.0021	112.6
SARD-BOCA-BHIL	303.9	9.9	-39.68	25.65	29.6655	-35.1386	-5.4731	110.4
SARD-PENT-BHIL	304.7	10.5	-37.99	20.20	60.3411	-26.9861	33.3550	98.2
PENT-BHIL-TRUC	305.5	10.6	1.80	22.84	71.8215	-34.0386	37.7828	122.0
BVAL-BHIL-VRDE	302.5	9.7	-29.22	17.65	25.3397	-46.0633	-20.7236	102.2
SARD-BHIL-VRDE	302.9	9.7	-40.55	26.24	27.3724	-37.1820	-9.8097	112.5
P149-PENT-BOCA	304.0	10.1	-46.43	12.35	48.6976	-26.1769	22.5207	95.3
BVAL-PENT-BOCA	303.7	10.3	-46.93	18.30	48.4954	-50.3774	-1.8820	93.8
PERA-P149-BOCA	304.4	10.0	-49.35	17.26	45.9998	-29.0466	16.9532	98.4
SARD-GIRL-BOOM	304.4	9.3	-13.58	23.38	42.0777	-55.4894	-13.4118	87.1
SARD-VRDE-P150	302.8	9.7	-42.21	23.53	24.0197	-43.9714	-19.9518	108.1

greatest horizontal extension. The least horizontal extension is on the short axis of the ellipse.

CHAPTER FOUR

Discussion

Overview

The seismo-lineament analysis code produced seismo-lineaments associated with fourteen earthquake focal mechanisms. Six of these seismo-lineaments overlap the suspected trace of the DVF. Those six earthquake events are tentatively correlated to the DVF. A structural-geomorphic analysis of high resolution hillshade images took place in the area encompassed by all six seismo-lineaments. This analysis produced 28 geomorphic indicators of faulting that might have been formed by sinistral movement on the DVF. Field work in the seismo-lineament produced data for faults that had not been previously mapped. These geomorphic indicators of faulting and the faults measured in the field occur on a line trending 38°±3° over a lateral distance of 12.5 kilometers with minor deviations to the northwest and southeast. This chapter is intended to provide interpretations based on the SLAM analysis, field work, and GPS crustal strain analysis.

Spatial Correlation of Earthquakes with the Dog Valley Fault

The only earthquake that has been correlated with the DVF previous to this study is S1, the 1966 M6.0 Truckee earthquake that was used to define the DVF. This research spatially correlates an additional five earthquakes to the DVF. These are S2, S3, S5, S8, and S11. Focal mechanism data for each of these earthquakes produces a seismo-lineament that overlaps with the seismo-lineament of S1 and encompasses > 90% of the DVF as mapped by USGS (2017). The relocated hypocenters for these events range from

0.368 km to 10 km below sea level with an average depth of 6.7 km. A composite seismo-lineament was made by layering the seismo-lineaments of these six events as shown in Figure 44. The ground surface trace of the DVF should be inside of this composite seismo-lineament. The red curve in this figure connects all 28 geomorphic indicators of faulting located in this study.

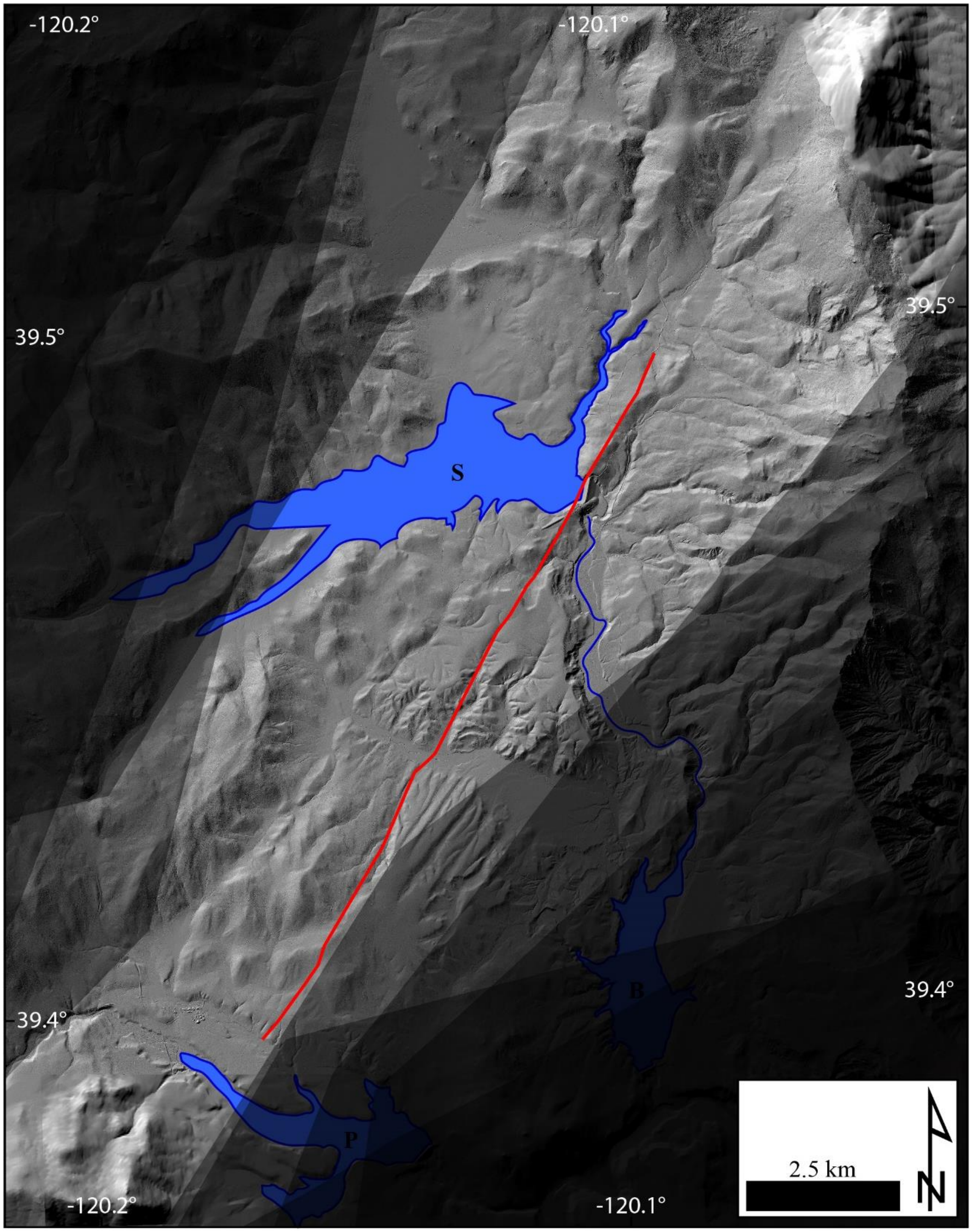

Figure 44. Composite seismo-lineament associated with S1, S2, S3, S5, S8, and S11 with the trend of all geomorphic indicators found in this study.

Field Interpretations

There are 28 features resulting from the structural-geomorphic analysis that are possible indicators of faulting. The features have been tentatively correlated to the DVF and their trend is similar to the expected trace of this fault based on available focal mechanism data and aftershock locations (Ryall et al., 1968; Greensfelder et al, 1968; Tsai and Aki, 1970). The red curve in Figure 44 intersects all 28 of the geomorphic indicators of faulting. Horizontal shear striations were found in F8SD, F4ND, and F2RW. Movement along these faults is inferred to be left lateral, consistent with the DVF. F8SD and F4ND are within 50 meters of the upstream face of the Stampede Dam on either side. Faults F1RE, F2RW, F4ND, F7PF, and F8SD are tentatively correlated to the DVF based on their orientation, inferred movement, and location inside the composite seismo-lineament.

Previous studies of the DVF suggest it is concealed (Hawkins et al., 1986; Greensfelder, 1968; Tsai and Aki, 1970). This study produced data for 5 faults in line with 28 geomorphic indicators of faulting. All five faults are within 1.5 km of the Stampede Dam and do not offer control points along this line south of the Stampede Dam structure. The DVF does not appear to break the surface along the entire length of the fault.

Hawkins et al. (1986) reports a northeast trending fault beneath the north abutment of the Stampede Dam with 3 to 9 meters of clayey gouge. As this is the only data available for this large fault beneath the dam there is no way to analyze strike and dip in conjunction with the DVF or faults found in this research. The limited data do suggest spatial correlation with the DVF based on the location and the general orientation of this buried fault.

There might be a fault in the draw directly northwest of the north abutment of the dam. This area was trenched in two places with 12' long trenches reaching a maximum depth of 0.9 m. These trenches could be expanded with better equipment and more time. If the trenches were more laterally extensive and deeper it might be discovered that a fault similar to F4ND is responsible for the location of the draw as well as the apparent lateral offset in stratigraphic units.

The search for geomorphic indicators of faulting might yield more data if performed on the point cloud instead of a hillshade image created from a 1 meter resolution digital elevation model (DEM). In the process of creating a DEM the LiDAR data collected in flight paths are stitched together and linear topographic deviations are removed to smooth the elevation model and remove seams in between different flight paths. This smoothing process might remove linear topographic deviations created by the DVF. Future works might find it more useful to analyze the point cloud data for geomorphic indicators of faulting as an alternative to an improved hillshade image sourced from a DEM.

The structural-geomorphic analysis process involves a visual inspection of the ground elevation model to find topographic lineaments that agree with the seismo-lineament swath. This visual inspection for topographic lineaments could be automated. Several attempts were made to produce an automated process within ArcGIS to search for lineaments within a range of orientation via convolution filters. These attempts did not produce a viable automated search.

CHAPTER FIVE

Conclusions

The purpose of this research is to use the Seismo-Lineament Analysis Method to better constrain the ground surface trace of the Dog Valley Fault. This research utilized 14 focal mechanism solutions (NCEDC, 2017) and relocated earthquake hypocenters (Waldhauser, 2017) in the current version of the Seismo-Lineament Analysis code (Cronin, 2008; Cronin, 2014) to produce seismo-lineaments that constrain the area where the DVF might intersect the ground surface. Five earthquakes were spatially correlated with the DVF. A LiDAR based geomorphic analysis of the overlap in the six seismo-lineaments revealed 28 geomorphic indicators of faulting. These features are in line with five northeast trending near vertical faults measured in the field. These faults are tentatively correlated with the DVF based on their location, and orientation. Three of these faults occur within 50 meters of the upstream face of the Stampede Dam.

The best constraint for the ground surface trace of the DVF available from the data presented in this study is shown in Figure 45. This map is a compilation of seismo-lineaments, features located in the structural-geomorphic analysis, and fault data collected in the field. The red curve intersects all structural geomorphic indicators of faulting as well as faults found in this research. The curve is solid where faults were measured, and dashed where no faults were found. This curve trends 38°±3° for 12.5 kilometers from the northwestern most arm of Prosser Creek reservoir through the north abutment of the Stampede Dam and towards Dog Valley.

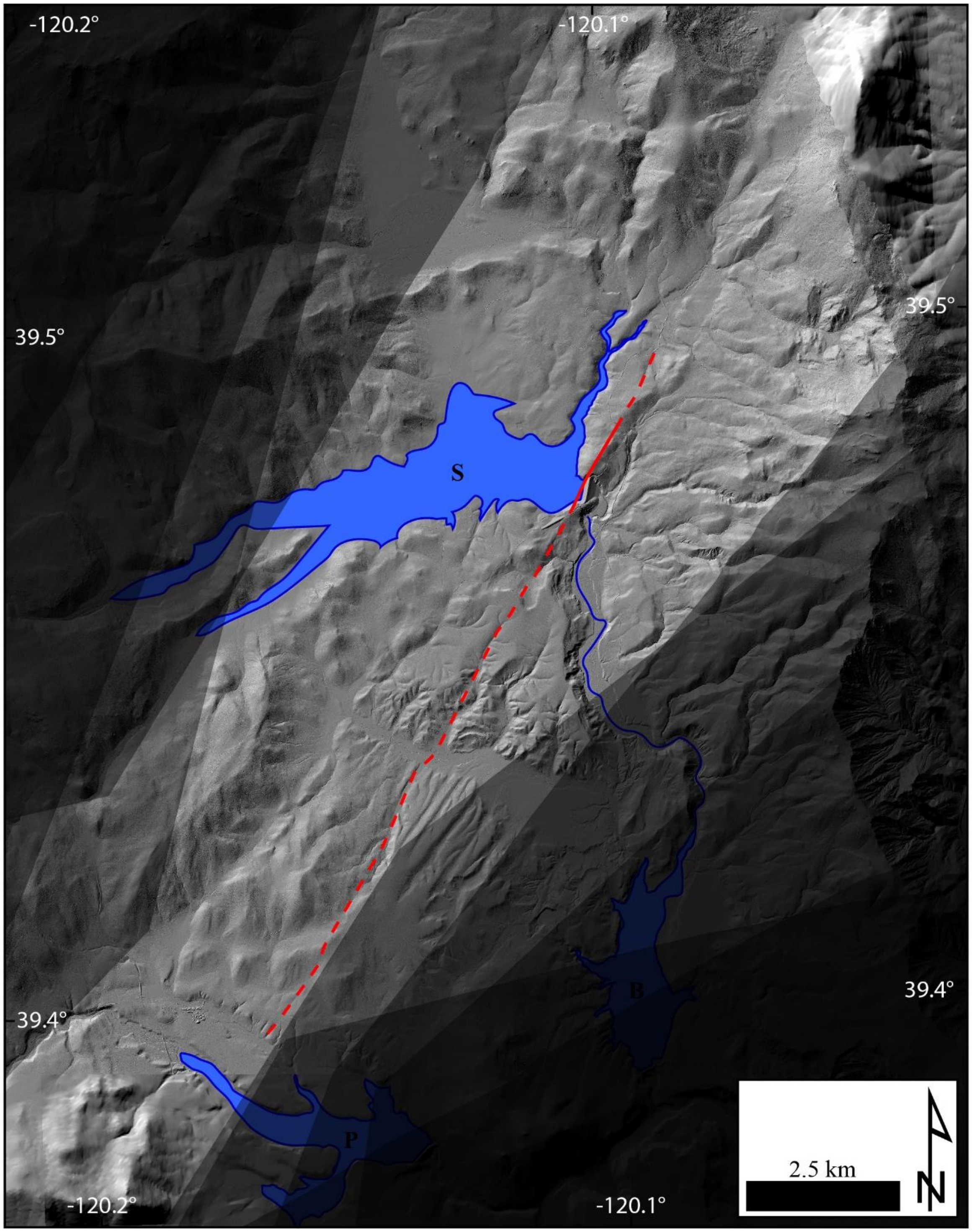

Figure 45. Possible location for the ground surface trace of the DVF based on seismo-lineaments, structural-geomorphic analysis, and faults found during field work. The curve is solid where faults are measured and dashed where no faults are found.

REFERENCES

Argus, D.F., and Gordon, R.G., 1991, Current Sierra Nevada-North America motion from very long baseline interferometry – Implications for the kinematics of the western United States: Geology, v. 19, p. 1085-1088.

Ashburn, J.A., 2015, Investigation of a lineament that might mark the ground-surface trace of the Dog Valley Fault, Truckee area, northern California: Baylor University, B.S. thesis, available via http://CroninProjects.org/Vince/AshburnBSThesis2015.pdf.

Bonilla, M.G., 1982, Evaluation of potential surface faulting and other tectonic deformation: U.S. Geological Survey Open-File Report 82-732, p. 58.

Blewitt, G., Kreemer, C., Hammond, W.C., and Goldfarb, J.M., 2013, Terrestrial reference frame NA12 for crustal deformation studies in North America: Journal of Geodynamics 72:11–24. doi:10.1016/j.jog.2013.08.004.

Blewitt, G., 2015, Terrestrial reference frame requirements for studies of geodynamics and climate change: International Association of Geodesy Symposia, DOI 10.1007/1345_2015_142.

Blewitt, G., Kreemer, C., Hammond, W.C., and Gazeaux, J., 2016, MIDAS robust trend estimator for accurate GPS station velocities without step detection: Journal of Geophysical Research, doi: 10.1002/2015JB012552.

Burbank, D.W. and Anderson, R.S., 2001, Tectonic geomorphology: Blackwell Science, Oxford, p. 274.

Cronin, V.S., 2008, Finding the mean and 95 percent confidence interval of a set of strike-and-dip or lineation data: Environmental and Engineering Geoscience, v. XIV, no. 2, p. 113-119.

Croinin, V.S., 2012, Excel spreadsheet for computing infinitesimal strain from GPS velocity data from sites in a triangular array: available via http://croninprojects.org/Vince/GPS-strain/gps_strain_calculator_excel.xls.

Cronin, V.S., 2014, Seismo-Lineament Analysis Method (SLAM), using earthquake focal mechanisms to help recognize seismogenic faults: Proceedings of the 5th International INQUA meeting on Paleoseismology, Active Tectonics and Archeoseismology (PATA Days), 21-27 September, Busan, South Korea, p. 21-27 September 2014, p. 28-31, ISBN 9791195344109 93450; available via http://croninprojects.org/Vince/SLAM/CroninINQUA_PATA14.pdf.

Cronin, V.S., and Resor, P., 2016, GPS, strain, and earthquakes: Science Education Resource Center and UNAVCO, GETSI Project, available via http://serc.carleton.edu/getsi/teaching_materials/gps_strain/index.html.

Cronin, V.S., and Sverdrup, K.A., 2003, Multiple-event relocation of historic earthquakes along Blanco Transform Fault Zone, NE Pacific: Geophysical Research Letters, v.30 (19), doi: 10.1029/2003GL018086.

Cronin, V.S., Millard, M., Seidman, L., and Bayliss, B., 2008, The Seismo-Lineament Analysis Method (SLAM) -- A reconnaissance tool to help find seismogenic faults: Environmental and Engineering Geology, v. 14, no. 3, p. 199-219. Available via http://eeg.geoscienceworld.org/cgi/content/abstract/14/3/199.

Cronin, V.S., Schurter, G., and Sverdrup, K.A., 1993, Preliminary Landsat lineament analysis of the northern Nanga Parbat-Haramosh Massif, northwest Himalaya: Geological Society of London Special Publication, no. 74, p. 193-206.

DeMets, C., Gordon, R.G., and Argus, D.F., 2010, Geologically current plate motions: Geophysical Journal International, doi: 10.1111/j.1365-246X.2009.04491.x246X.2009.04491.x

Dixon, T.H., Miller, M., Farina, F., Wang, H.Z., and Johnson, D., 2000, Present-day motion of the Sierra Nevada block and some tectonic implications for the Basin and Range province, North American Cordillera: Tectonics, v. 19, p. 1-24.

DWR, 2017, Daily reservoir storage summary: Department of Water Resources, California Data Exchange Center, accessed 8 June 2017 via https://cdec.water.ca.gov/cgi-progs/reservoirs/RES.

Early, D., Noack, S., Clark, E., Heyd, T., Markell, C., Kos, R., Press, S., and Boutillier, S., 2006, 2025 general plan for the Town of Truckee: available via http://laserfiche.townoftruckee.com/weblink/0/doc/59259808/Page1.aspx.

Fisher, R.A., 1953, Dispersion on a sphere: Proceedings Royal Society, London, v. A217, no. 1130. p. 295-305.

Greensfelder, R., 1968, Aftershocks of the Truckee, California earthquake of September 12, 1966: Bulletin of the Seismological Society of America, v. 58, no. 5, p. 1607-1620.

Hammond, W.C., Blewitt, G., and Kreemer, C., Block modeling of crustal deformation of the northern Walker Lane and Basin and Range from GPS velocities: Journal of Geophysical Research, v. 116, B04402, doi: 10.1029/2010JB007817.

Hawkins, F.F., LaForge, R. and Hansen, R.A., 1986, Seismotectonic study of the Truckee/Lake Tahoe area northeastern Sierra Nevada, California for Stampede, Prosser Creek, Boca, and Lake Tahoe dams: U.S. Bureau of Reclamation Seismotectonic Report No. 85-4, 210 p.

Hunter, L.E., Howle, J.F., Rose, R.S., and Bawden, G.W., 2011, LiDAR-assisted identification of an active fault near Truckee, California: Bulletin of the Seismological Society of America, v. 101, no. 3, p., 1162-1181, doi:10.1785/0120090261.

InfoSearch International, 2007, 2006 Reno-Sparks visitor profile study: available via https://www.visitrenotahoe.com/about-us/marketing/research_reports.html.

Kachadoorian, R., Yerkes, R.F., and Waananen, A.O., 1967, Effects of the Truckee, California, earthquake of September 12, 1966: U.S. Geological Survey, Circular 573, p. 14.

Kreemer, C., Holt, W.E., and Haines, A.J., 2003, An integrated global model of present-day plate motions and plate boundary deformation: Geophysical Journal International, v. 154, p. 8-34.

Kreemer, C., and Hammond, W.C., 2007, Geodetic constraints on areal changes in the Pacific-North America plate boundary zone – What controls Basin and Range extension?: Geology, v. 35, no. 10, p. 943-947.

Kreemer, C., Blewitt, G., and Hammond, W.C., 2009, Geodetic constraints on contemporary deformation in the northern Walker Lane – 2 Velocity and strain rate tensor analysis, *in* Oldow, J.S., and P.H. Cashman, [editors], Late Cenozoic Structure and Evolution of the Great Basin – Sierra Nevada Transition: Geological Society of America, Special Paper 447, p. 17-31.

Lindsay, R., 2012, Seismo-lineament analysis of selected earthquakes in the Tahoe-Truckee area, California and Nevada: Baylor University, M.S. thesis, available via https://baylor-ir.tdl.org/baylor-ir/handle/2104/8441.

McCalpin, J., ed., 2009, Paleoseismology [2nd edition]: Amsterdam, Academic Press, 613 p.

Miller, V.C., 1961, Photogeology: McGraw-Hill, New York, p. 248.

NCALM, 2014, Full waveform LiDAR survey of Tahoe National Forest: available via http://opentopo.sdsc.edu/raster?opentopoID=OTSDEM.032017.26910.2

NCEDC, 2017, Northern California earthquake data center: available via http://quake.geo.berkeley.edu/ncedc/catalog-search.html.

Nevada Geodetic Laboratory, 2017, The MAGNET GPS network, available via http://geodesy.unr.edu/magnet.php

NOAA, 2017, Observed precipitation map: accessed 11 May 2017, available via http://www.cnrfc.noaa.gov/archivePrecipMap.php?area=es&month=09&day=21&year=16.

Olig, S., Sawyer, T., Wright, D., Terra, F., and Anderson, L., 2005, Preliminary seismic source characterization of faults near Stampede and Prosser Creek dams – Washoe project and Boca Dam - Truckee storage project: U.S. Department of the Interior, Bureau of Reclamation, Denver, 65 p

Ray, R.G., 1960, Aerial photographs in geologic interpretation and mapping: U.S. Geological Survey Professional Paper 373, p. 230.

Reasenberg, P.A., and Oppenheimer, D., 1985, FPFIT, FPPLOT, and FPPAGE: Fortran computer programs for calculating and displaying earthquake fault-plane solutions: U.S. Geological Survey, Open-File Report, no. 85-739.

Reed, T.H., 2014, Spatial correlation of earthquakes with two known and two suspected seismogenic faults, north Tahoe-Truckee area, California: Baylor University, M.S. thesis, available via https://baylor-ir.tdl.org/baylor-ir/handle/2104/9097.

Ryall, A., Van Wormer, J.D., and Jones, A.J., 1968, Triggering of micro-earthquakes by earth tides, and other features of the Truckee, California, earthquake sequence of September, 1966: Bulletin of the Seismological Society of America, v. 58, no. 1, p. 215-248.

Scherbaum, F., Kuehn, N., and Zimmermann, B., 2013, Earthquake focal mechanism: Wolfram Demonstration Project, available via http://demonstrations.wolfram.com/EarthquakeFocalMechanism/

Schmidt, J., Leigh, A., and Parr, K. L., 2012, Stampede Dam safety of dams modification: U.S. Bureau of Reclamation, available via https://www.usbr.gov/mp/nepa/documentShow.cfm?Doc_ID=9930.

Scholz, C.H., 2002, The mechanics of earthquakes and faulting [2nd ed.]: Cambridge, U.K., Cambridge University Press, 471 p.

Schweickert, R.A., Lahren, M.M., Smith, K.D., Howle, J.F., and Ichinose, G., 2004, Transtensional deformation in the Lake Tahoe region, California and Nevada, USA: Tectonophysics, v. 392, p. 303-323.

Slemmons, D.B., and dePolo, C.M., 1986, Evaluation of active faulting and associated hazards, *in* Studies in Geophysics—Active Tectonics: National Research Council, National Academy Press, Washington, D.C., pp. 45–62.

Tsai, Y-B., and Aki, K., 1970, Source mechanism of the Truckee, California earthquake of September 12, 1966: Bulletin of the Seismological Society of America. v. 60, no. 4, p. 1199-1208.

USACE, 2008, SPK_20080922-26: accessed September 2016 via https://griduc.rsgis.erdc.dren.mil/

UNAVCO, 2017, Plate boundary observatory, available via http://pbo.unavco.org/network/gps.

USGS, 2016, National elevation dataset: accessed April 2016, available via http://ned.usgs.gov.

USGS, 2017, Quaternary fault and fold database of the United States: available via http://earthquake.usgs.gov/hazards/qfaults/.

Waldhauser, F., 2009, Near-real-time double-difference event location using long-term seismic archives, with application to northern California: Bulletin of the Seismic Society of America, v. 99, no. 5, pp. 2736-2748, doi: 10.1785/0120080294.

Waldhauser, F., 2017, Real-time double-difference earthquake locations for northern California, available via http://ddrt.ldeo.columbia.edu.

Waldhauser, F. and Schaff, D.P., 2008, Large-scale relocation of two decades of northern California seismicity using cross-correlation and double-difference methods: Journal of Geophysical Research, v. 113, B08311, doi: 10.1029/2007JB005479.

Wesson, R.L., Helley, E.J., Lajoie, K.R. and Wentworth, C.M., 1975, Faults and future earthquakes, *in* Borcherdt, R.D., [editor], Studies for seismic zonation of the San Francisco Bay region: U.S. Geological Survey Professional Paper 941-A, p. 5-30.

Worrell, V.E., 2014, The Seismo-Lineament Analysis Method (SLAM) applied to the South Napa earthquake and antecedent events: Baylor University, M.S. thesis, available via https://baylor-ir.tdl.org/baylor-ir/handle/2104/9796.